Master in Chemical Engineering

A thermographic setup for real-time monitoring water in PEM fuel cells – from proof of concept to laboratory tool

A Master's dissertation

by

Gerson Tristão de Sousa

Developed within the course of Dissertation

Held in

DLR: Institute of Technical Thermodynamics

German Aerospace Center

Supervisor at FEUP: **Prof. Adélio Mendes**

Supervisor at DLR: **Dr. Indro Biswas**

U.PORTO
FEUP FACULDADE DE ENGENHARIA UNIVERSIDADE DO PORTO

Chemical Engineering Department

lepabe Laboratory for Process Engineering, Environment, Biotechnology and Energy

FCT REPÚBLICA PORTUGUESA

fevereiro de 2020

Acknowledgments

I am very grateful to my supervisor at DLR, Dr. Indro Biswas and Prof. Adélio Mendes, for all their support, motivation, time and for constantly pushing me outside my comfort zone, which makes me evolve in every way, and makes me learn more than ever I imagine.

To Indro, thank you so much for always listen to my doubts, questions or suggestions, and help me in every way that possibly I could be helped and for always give to me the freedom to put in practise my ideas. Always with a good mood, even if I was having a bad day, after a small talk, I was right away with a smile in my face.

Professor Adélio Mendes, supervisor of this master's dissertation, is an intergrated member of LEPABE – Laboratório de Engenharia de Processos, Ambiente, Biotecnologia e Energia, funded by the research unity UID/EQU/00511/2019 – Laboratório de Engenharia de Processos, Ambiente, Biotecnologia e Energia – LEPABE – funded by national funds through FCT/MCTES (PIDDAC). To professor Adélio, I want to express my gratitude for helping me whenever it necessary and to push me and motivate me to think for myself to solve the different problems that were appearing during the work. For the many important calls with the suggestions that really helped me in the time I need most.

I want to thanks to Sofia Delgado and Tiago Lagarteira for helping me before starting this adventure, providing me first knowledge about the big topic I was going to face. Thanks again to Sofia for the times I disturb with some doubts, showing always available to answer to any question.

I am grateful to the whole electrochemistry group, that in different moments were always available to help the best way possible: Torsten Knöri, Mathias Schulze, Peter Mahnke, Krishan, Pia, Daniel Garcia, Jens and Siggy for all the contribution you provide to enriched all my experience in DLR. I want to thanks to Christina Schmitt for the XPS and XRD measurements that I needed. A special thanks to Julian for all company, discussions and sharing moments during these months, it was important to me work alongside you and at the same time, making a friendship for life.

During this wonderful and very difficult journey I want to thank all my friends and family for the constant support, academically or emotionally, listening and even visit me some days, that was important to release the daily stress and just appreciate other important moments too.

I want to thanks to my mom too, for being my mom. Every time I need a wise word, every time I need some advice, some difficult decision, she is always there to support me, even with the distance, showing all the time the unconditional love that always characterized you.

And finally, a very special thanks to Camylla for the all support, patience and caring in the most difficult moments, in the moments I was less confident and just projecting dark moments in my work, you were the first believing in me and my potential, you were the first showing me some light inside me, capable of anything and overcome any obstacle. With all your support and love, every difficult moment seemed much easier.

Abstract

Fuel cells and in particular proton exchange membrane fuel cells are an important part of a promising technology to provide a completely clean energy. It is a technology in constant development and study to become economically viable. The main issues are related to the platinum loading, due to the high cost of platinum, and water management, since improving the performance of this fuel cell type heavily depends on the study of water management within the cell. To better understand water (and heat) phenomena, thermography is being developed as a method of characterization of condensed water in fuel cells. This novel and ex-situ technique can offer a good understanding about liquid water flow in the flowfield channels and realise the exact reasons that compromise the performance. It can also offer the possibility of, with a close view and a good resolution, to create a temperature profile along and across the channels to study the heat distribution.

This work focus in developing of a thermography method based on an anti-reflective coating germanium window especially transparent to the relevant infrared spectrum. This window revealed clear images of the condensed water at the flowfield channels. To incorporate the germanium window, some adaptations in the fuel cell design needed to be done and these adaptations needed to be made so that the cell remain tight.

Thermography proved to be very advantageous for analysing the condensed water in the channels, with or without magnification. Without magnification, it was possible to observe an overview of the flowfield and detect regions where water preferably accumulates. Magnified images allow a more detailed observation of the liquid water along the channels, which is important for a future study about transport water phenomena. With this method, water and heat management in proton exchange membrane fuel cells are closer to be completely understood and, in future work, tune the cell components to achieve better performance and long-life operation.

Key words: fuel cell, PEMFC, thermography, water management, infrared, germanium, anti-reflective coating

Resumo

As células de combustível e em particular as células de combustível com membrana de permuta protónica (PEMFC) fazem parte de uma tecnologia promissora para fornecer energia completamente limpa. É uma tecnologia em constante estudo e desenvolvimento para se tornar economicamente viável. Os principais problemas estão relacionados com a quantidade de platina utilizada, devido ao elevado custo da mesma, e à gestão de água, uma vez que melhorar o desempenho deste tipo de célula de combustível depende do estudo da gestão da água na célula. A termografia está a ser desenvolvida como um método de caracterização da água condensada nas células de combustível e, assim, entender melhor os fenómenos relacionados com a água (e calor). Esta técnica inovadora e ex-situ pode propiciar um bom entendimento sobre o transporte da água no estado líquido nos canais e, deste modo, saber exactamente as razões que comprometem o seu desempenho. Também pode dar a possibilidade de, com uma boa resolução e uma vista aproximada, criar um perfil de temperaturas ao longo dos canais para estudar a distribuição de calor.

Este trabalho foca no desenvolvimento da termografia baseado numa janela de germânio revestida com um anti reflector especialmente transparente para o espectro de infravermelhos utilizado, revelando imagens nítidas da água condensada no campo de canais. Para incorporar esta janela de germânio, algumas adaptações no desenho da célula precisaram de ser feitas e estas adaptações foram necessárias para que a célula permanecesse apertada.

A termografia provou ser vantajosa na análise da água condensada no campo de canais, com e sem ampliação. Sem ampliação, é possível observar uma vista geral do campo de canais e detectar regiões onde a água preferencialmente se acumula. As imagens com ampliação permitem uma observação mais detalhada da água no estado líquido ao longo dos canais, que é importante para um estudo futuro sobre o fenómeno de transporte de água nas células de combustível. Com este método, a gestão da água e do calor nas células de combustível com membrana de permuta protónica estão mais perto de serem completamente entendidas e, num estudo futuro, ajustar os componentes da célula para obter um melhor desempenho e um tempo de operação mais longo.

Palavras-chave: células de combustível, PEMFC, termografia, gestão da água, infravermelho, germânio, revestimento anti reflector

Declaration

I hereby declare, on my word of honour, that this work is original and that all non-original contributions were properly referenced with source identification.

Sign and date

Gerson Tristão de Sousa

February 10th 2020

Table of contents

List of figures

List of tables

Notation and Glossary

Latin Letters

c	Speed of light	$m \cdot s^{-1}$
d_w	Wien's displacement constant	$\mu m \cdot K$
e	Emissivity	
E_{Thermo}	Thermodynamic equilibrium potential	V
E	Total emissive power	$W \cdot m^{-2}$
E_λ	Spectral emissive power	$W \cdot m^{-3}$
F	Faraday constant	96485 $C \cdot mol^{-1}$
G	Gibbs free energy	J
h	Planck constant	$6.6 \cdot 10^{-34}$ $J \cdot s$
k	Boltzmann constant	$1.38 \cdot 10^{-23}$ $J \cdot K^{-1}$
n	Number of moles of electrons transferred	mol
n	Refractive index	
P	Pressure	bar
R	Universal gas constant	$J \cdot mol^{-1} \cdot K^{-1}$
T	Temperature	K

Greek Letters

λ	Water Content	
λ	Wavelength	μm
λ_{max}	Wavelength for maximum radiation intensity	μm
σ	Stefan-Boltzmann constant	$5.67 \cdot 10^{-8}$ $W \cdot m^{-2} \cdot K^{-1}$
τ	Transmissivity	

List of Acronyms

BPP	Bi-Polar Plate
CCM	Catalyst Coated Membrane
CL	Catalyst Layer
EU	European Union
FLIR	Foward Looking Infrared
FTIR	Fourier Transformed Infrared
GDL	Gas Diffusion Layer
GHG	Green House Gases
IR	Infrared
HOR	Hydrogen Oxidation Reaction
LWIR	Long Wavelength Infrared
MEA	Membrane Electrone Assembly
MPL	Micro Porous Layer
MWIR	Middle Wavelength Infrared
ORR	Oxygen Reduction Reaction
PEM	Polymer Electrolyte Membrane
PEMFC	Proton Exchange Membrane Fuel Cell
PTFE	Polytetrafluoroethylene
RH	Relative Humidity
XPS	X-Ray Photoemission Spectroscopy
XRD	X-Ray Difraction

1 Introduction

1.1 Framing and presentation of the work

At the present, the conscience of governments and society is increasing in order to provide a sustainable planet for all of us now and in the future. In the energy sector, since the energy demand is increasing with time, the concerns about depleting fossil fuels, greenhouse gases emission (GHG), global warming and energy security are increasing too, leading the governments to set targets for more investment in renewable resources and eventually replace entirely. For example, European Union (EU) set for 2020 three key energy targets, the reduction of 20% in GHG emissions from 1990 levels, 20% of EU energy from renewable sources and 20% improvement in energy efficiency [1]. According to International Energy Agency, from 1990 to 2017 there was an increase in primary energy demand from 8 765 to 13 971 Mtoe [1]. In Figure 1 is illustrated the primary energy by source worldwide, in 1990 and 2017.

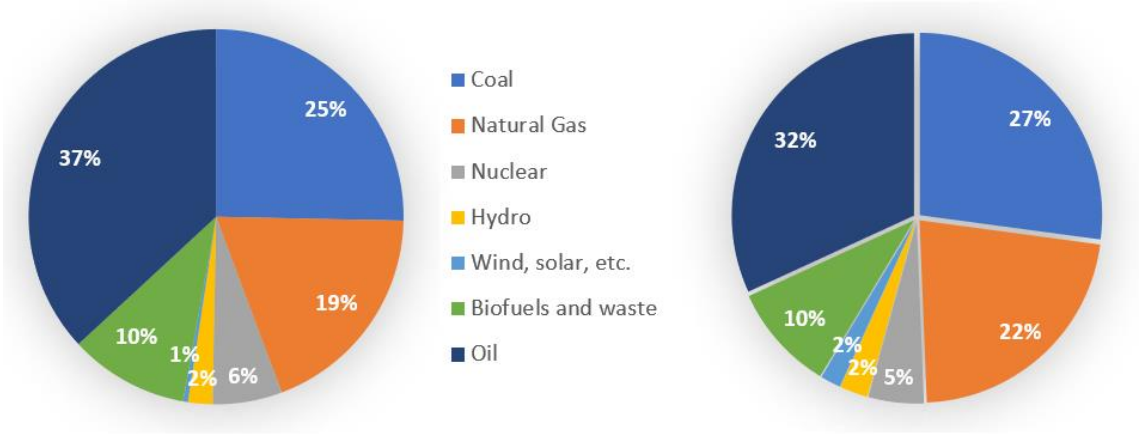

Figure A.1. ***Primary energy supply by source in the World (1990 and 2017). (Adapted from [1])***

All these environment concerns promote the development of novel technologies with high conversion efficiencies and low or zero emissions, with respect to GHG and other pollutants. Hydrogen energy systems as fuel cells seem to be one of the solutions to provide a sustainable environment. The first fuel cell was created in 1839 by William Grove [2]. Various fuel cells theories were studied during nineteenth and twentieth century but only in 1960s was started an extensive fuel cell research by NASA and now fuel cells technologies have seen a revival in recent years. Nowadays, fuel cell technology can be used in transport sector. This sector is responsible for a large amount of GHG emissions. Transport vehicles could be fuelled by hydrogen gas produced using electricity from intermittent renewable sources, producing only water vapour as a by-product and could then eliminate nearly all particulate matter and GHG emissions associated with the sector as well as provide added value to excess electricity from

renewable resources during low demand. In this context, the installation of new supply infrastructures for alternative fuels, e.g. hydrogen, is an important additional economical political factor. Dedicated analysis has clearly shown that energy conversion in fuel cells has to be based on fuels, in particular hydrogen, derived from renewable sources, to provide a full clean energy [3].

Among the fuel cells, the proton exchange membrane fuel cells (PEMFC) is a desirable technology because it operates at low temperatures, include quick start-up and shut-down capabilities, it is comparatively simple in their construction and it has the potential for high volume manufacturing, making it attractive specially for vehicle application. Nevertheless, there are several challenges as cost, lifetime under real conditions and infrastructure to supply high purity hydrogen that need to be overcome to be an economically viable technology to proceed towards full commercialisation. Since PEMFC operates at low temperatures, there will be necessarily liquid water in the cell, so the water management is one of the most important and critical topics in this technology. An optimum balance of water is needed since on one hand the membrane needs to be hydrated and on other hand an excess of water will provoke water flooding within the cell.

Currently, there are some techniques to analyse temperature and water management in situ. However, some phenomena are not completely understood, so there are a continuously search for techniques to understand better these phenomena and then improve the PEMFC technology. Thermography, as an imaging technology that monitors by thermal radiance emitted by a surface, can be explored to observe directly into the cell to study heat and water management. Thermography allows an analysis outside the system, so it not interferes with the fuel cell system itself. With the direct looking through the fuel cell it could be possibly understand better how the water or the heat distributes or how the water flows in the flowfield channels and the correlation with the performance, allowing improvements in order to achieve better performances and more viable fuel cells.

There was a previous work focus on the magnification limit of a low-cost infrared camera to visualize the PEMFC flowfields [4]. This work will focus on the development of the adaptation of the cell to incorporate the germanium window and to detect the different problems that this adaptation brings. Besides that, this work will show the benefits of use the anti-reflective coated germanium for optics purposes.

1.2 Presentation of the institution

The German Aerospace Center (Deutsches Zentrum für Luft- und Raumfahrt; DLR) is the national aeronautics and space research centre of the Federal Republic of Germany. Its extensive research and development work in aeronautics, space, energy, transport, security

and digitalisation is integrated into national and international cooperative ventures. In addition to its own research, as Germany's space agency, DLR has been given responsibility by the federal government for the planning and implementation of the German space programme. DLR has approximately 7700 employees at 16 locations in Germany: Cologne (headquarters), Augsburg, Berlin, Bonn, Braunschweig, Bremen, Goettingen, Hamburg, Juelich, Lampoldshausen, Neustrelitz, Oberpfaffenhofen, Stade, Stuttgart, Trauen, and Weilheim. DLR also has offices in Brussels, Paris, Tokyo and Washington D.C.

In Stuttgart, the DLR is situated in Pfaffenwaldring 38-40 and employs around 700 members of staff at its six institutes. Here, the main research areas are high-performance composite structures, new road and rail vehicle concepts, laser system development, energy storage concepts, gas turbines, and technologically advanced combustion processes, as well as the development of receivers for solar thermal power plants. DLR Stuttgart has 6 Institutes: Institute of Structures and Design, Institute of Vehicle Concepts, Institute of Technical Physics, Institute of Engineering Thermodynamics, Institute of Combustion Technology and Institute of Solar Research. The present work was developed in the Institute of Engineering Thermodynamics, composed by a staff of 180 scientific and technical employees, engineers and doctoral candidates dedicated to research in the field of efficient energy storage systems that conserve natural resources, and next generation energy conversion technologies. Within this Institute, the present work was developed in the Department of Electrochemical Energy Technology, headed by Prof. K. Andreas Friedrich, with a team of 60 people on the development of efficient electrochemical energy converters, primarily batteries, fuel cells and electrolysers. [5]

1.3 Contribution to the work

In PEMFC, there are some phenomena as water management or heat distribution that are not completely understood and influence the performance of the cell. The thermography can be useful to observe directly the heat distribution and water formation and flow within the cell and it is possible to create a map of water and heat distributions without interfere directly in the cell, working as a diagnostic technique. With this observation is possible to better explain the interaction of different mechanisms and improve some fuel cell components and leading this technology to be a viable market option as a clean sustainable energy source. In practise, this technique has a great potential for magnified and non-magnified setups. The work has the purpose of improve the fuel cell setup available for a good thermography evaluation, identifying several limitations, some improved at the moment and others for further improvement.

1.4 Organization of the thesis

This thesis is divided into five distinct chapters. The first one, the introduction, gives the reader a context of the purpose of the work. The second chapter, the state of art, the author describes the information related with PEMFC technology including history, latest advances and challenges of this technology and presents the theory of physical concepts necessary for the thermographic viewing. The third chapter, the materials, it is explained the fuel cell and test-bench and software used for this work, as the optical materials needed to optical system analyses, as infrared camera and window placed in the cell. The fourth, the results, include applications and limitations of thermography and it is where is presented the different limitations founded and the improvements necessary for further application. Finally, the fifth and last chapter presents the conclusion of the work and some suggestions for future work developments and optimization.

2 State of the art

A fuel cell is an electrochemical device that converts free energy into electrical energy, provided by the fuel (e.g. hydrogen) and the oxidant (e.g. oxygen from the air). In a typical fuel cell, gas fuels are fed continuously to the anode (negative electrode), while an oxidant is fed continuously to the cathode (positive electrode) and a electrochemical reaction takes place at each electrode to produce an electric current.

Hydrogen and fuel cell systems are starting to be incorporate in transport sector and stationary power sector. In transport technology, fuel cells provide a low-carbon option (when the hydrogen is produced from renewable energy sources), the driving performance and refuelling is comparable to conventional vehicles, has high-utilisation in road vehicles (trucks and buses), trains, ferry boats and utilitarian vehicles (e.g. forklifts) [6]. Fuel cells and batteries compete in some market segments in transport technology. However, in the context of the energy transition, fuel cells and batteries should be complementary because batteries are highly appropriated to smaller and lighter vehicles travelling short distances, while fuel cells are more suitable for heavier vehicles travelling over longer distances and high utilisation rate vehicles, for example taxis [6]. Furthermore, to reach the most economical long-term option, it is a possibility these two technologies combine each other (flexibility of hydrogen and efficiency of batteries) [6]. This complementarity is demonstrated in Figure 2, including the bio and hydrogen-based synthetic fuels to fuel cells and batteries.

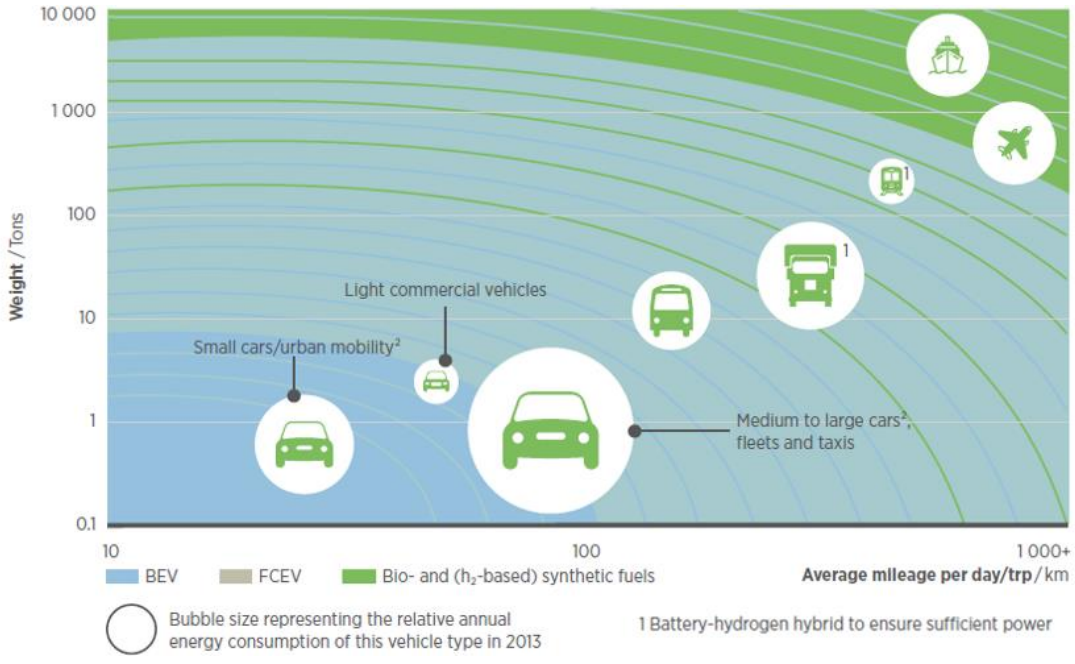

Figure 1. Segmentation of the transport market (Adapted from [6]).

In stationary power sector, fuel cells can be incorporated in uninterruptible supply or power backup systems for network equipment and datacentres or non-centralized power (e.g. in isolated regions or islands). Although it is more expensive and show worse roundtrip efficiencies comparing to batteries, hydrogen storage and fuel cells have a longer lifetime and temperature tolerance (useful in more extreme climates), making a good option for storing many hours of electricity supply in situations that is need large amounts of energy [6].

Fuel cells can be classified in two different ways, by the nature of the electrolyte and by the temperature range of operation. There are 6 different fuel cell types according to the nature of the electrolyte, where each one requires different electrode materials, temperature range or fuel type. These types can be grouped in acidic (with proton conduction) or alkaline (with anion conduction) fuel cells. According to the temperature range of operation, there are low temperature fuel cells, between 60 and 200 ºC and high temperature fuel cells, between 650 and around 900 ºC. The gap between 200 and 650 ºC is related to the unavailability of electrolytes in this temperature range.

Among these fuel cell types is Proton Exchange Membrane Fuel Cell (PEMFC) that operates at low temperature from 20 ºC until 80 ºC. Comparing with the other fuel cell types, it has higher achievable specific and volumetric power density and a quicker start-up. It is of special interest for transportation, as refuelling with hydrogen can be done within minutes, and the range can be increased by a large tank instead of the battery of a battery-only car [7]. An increase in market penetration of PEMFC vehicles, however, will depend on further production cost reductions as well as performance and durability improvements [8].

2.1 PEMFC

A PEMFC use as an electrolyte a proton exchange membrane, that is the heart of the fuel cell. PEMFC was first developed by General Electric in the USA in the 1960s for use by NASA on their first manned space vehicles and to provide the astronauts with clean drinking water [9] and also used by the U.S. Navy's Bureau of Ships (Electronics Division) and the U.S. Army Signal Corps. During the decades until nowadays there were several improvements in PEMFCs, closer than ever to commercialization of this technology. The main problems maintain the same, high cost and water management.

The PEMFC consists of two thin porous electrodes (anode and cathode) separated by a proton-conducting membrane which ionically connects the anode and the cathode, and it is sandwiched between two gas diffusion layers (GDLs) and two current collectors, the bi-polar plates (BPPs). At the anode of the cell, hydrogen is oxidized into protons and electrons by the hydrogen oxidation reaction (HOR), represented in Equation (1). The protons migrate through the membrane, with water into the cathode and electrons migrate to the cathode through an

external circuit, creating the electricity by electrical work. At the cathode, oxygen is reduced by the oxygen reduction reaction (ORR), represented in Equation (2), together with protons and electrons to produce water.

$$H_2 \rightarrow 2H^+ + 2e^- \quad (1)$$

$$\frac{1}{2}O_2 + 2H^+ + 2e^- \rightarrow H_2O \quad (2)$$

The overall reaction is:

$$H_2 + \frac{1}{2}O_2 \rightarrow H_2O \quad (3)$$

In this fuel cell type, the two reactants, in this case hydrogen and air, enter macroscopically by a channel in the bi-polar plate. It is connected to the flow field to distribute uniformly the reactant gases through the cell area to the GDL. The GDL will distribute the gases to the catalyst layer, where each reaction in each electrode happen. Both catalyst layers are separated by the polymer membrane that serves as the electrolyte, providing good ionic conductivity while maintain the separation of the reactant gases and prevent the flow of electrons through the membrane.

At the anode electrode, hydrogen gas molecules adsorb onto the supported catalyst material, usually platinum nanoparticles supported in carbon particles, which is used to help separate the hydrogen of its electron, oxidizing it to become a hydrogen proton (H^+). The proton formed is transported through the polymer electrolyte membrane (PEM) to the cathode electrode. Here, oxygen molecules are fed into cathode electrode, usually by supplying air. Like the active layer at the anode, appropriate nanosized catalyst particles are supported on electrically conducting porous materials. Once on the catalyst surface, the covalent bonds of oxygen molecule are broken, forming oxygen anions. The oxygen anions then combine with protons arriving through the membrane and with electrons that are used outside the fuel cell as electricity and water is produced.

2.2 Thermodynamics

The free energy of the chemical reaction that is converted into electrical energy by PEMFC is the energy available to do external work, neglecting the work done by pressure or volume changes and is related with the change in the Gibbs free energy, ΔG. The reaction in equation 3 is thermodynamically favoured because the Gibbs free energy of the products is less than that of the reactants. The free energy can be related with the reversible potential or potential in thermodynamic equilibrium by the Equation (4).

$$\Delta G = -nFE_{Thermo} \quad (4)$$

where *n* is the number of electrons involved in the reaction, *F* is the Faraday constant and E_{thermo} is the potential of the cell for thermodynamic equilibrium in the absence of a current flow, which means in open circuit.

The value of ΔG of the overall PEMFC reaction at standard conditions, ΔG^0, (25 ºC and 1 atm) is -237 kJ·mol^{-1}. The theoretical equilibrium potential, E_{thermo}, at standard conditions for hydrogen/oxygen fuel cell is 1.229 V [3].

$$E^0{}_{Thermo} = \frac{-\Delta G^0}{nF} = 1.229\,V \tag{5}$$

For temperatures and pressures different from standard conditions, the thermodynamic equilibrium potential can be calculated from the Nernst equation:

$$E = E^0 + \frac{RT}{2F} ln\left(\frac{P_{H_2} \times {P_{O_2}}^{0.5}}{P_{H_2O}}\right) \tag{6}$$

where *P* are the partial pressures of reactants and products (bar), *T* is the absolute temperature (K), *R* is the gases constant (J·mol^{-1}·K^{-1}) and *F* the Faraday's constant (C·mol^{-1}). [10]

The actual open circuit potential of a fuel cell is lower than the thermodynamic value due to reactants crossover from one electrode to the other through the electrolyte. Hydrogen crossover is more relevant than oxygen crossover because first, hydrogen molecules are smaller than oxygen ones, second, the platinum loading in the anode catalyst layer is lower than the cathode side, so it is easier for hydrogen molecules activate on catalyst sites in cathode than the opposite and third, ORR rate is lower than HOR. When hydrogen reaches the cathode side it will create parasitic reactions (HOR and hydrogen with direct contact with oxygen will react to create water), occupying part of the catalytic surface area dedicated to oxygen reduction, decreasing the cell performance [11].

The deviation of real potential from the thermodynamic potential is called overpotential or polarization. For PEMFC, there are three classifications of overpotentials which are activation, ohmic and mass transport overpotential, represented in Figure 2. Each one of then predominates at a certain interval of current density.

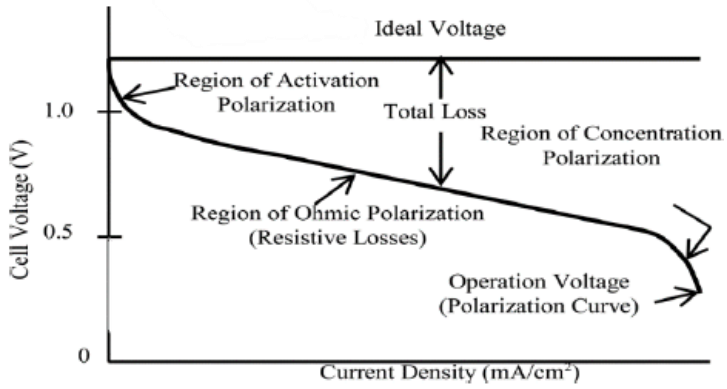

Figure 2. Typical fuel cell polarization curve (Adapted from [12]).

When current starts to flow, a deviation from the open circuit potential occurs corresponding to the energy that is needed to activate the anode and cathode reactions and corresponding to the electrical work performed by the cell. For PEMFC, which is composed of an acid membrane, the overpotential losses are much higher at the cathode because the ORR has slower kinetics than HOR [9]. The activation overpotential has more influence on low current densities.

The ohmic overpotential is generated due to electrical and ionic resistances, including the resistance in the membrane, electrodes, electrical bulk resistance in electrodes, GDLs and bi-polar plates, electrical contact between the catalyst layer and GDL and between GDL and bi-polar plate [13]. The ionic transport through the membrane is more difficult than the electronic charge transport. In a metallic conductor, in comparison, valence electrons associated with the atoms of the metal become detached and are free to move around the metal [3]. In a typical solid ionic conductor, the ions move from site to site, hopping through defects, interstitials or vacancies in the material. The number of charge carriers in an electronic conductor is much higher than a ionic conductor. In the polarization curve, the ohmic overpotential is illustrated by the straight line.

The mass transport overpotential is predominant at high current densities because reactants are being consumed at a faster rate than it takes for them to reach the catalyst surface. These losses are higher at cathode side because oxygen has to diffuse from the BPP to the flow field, through all the GDL length to the catalyst layer, with water and nitrogen molecules, because it is introducing air and not pure oxygen. Other possible factors are low porosity of the catalyst layer, an inadequate compression of the GDL and a high content of liquid water in the BPP channel. Some groups reported the increase of mass-transport losses at low relative humidification because of the low levels of hydration results in a reduced oxygen solubility and permeability in the ionomer [14, 15].

2.3 PEMFC Components

The different components of PEMFC can be grouped in two key groups, the membrane electrode assembly (MEA) and two bi-polar plates and flow field. The MEA is composed of a polymer electrolyte membrane, two catalyst layers and two gas diffusion layers.

2.3.1 Polymer Electrolyte Membrane (PEM)

In PEMFC, the membrane is a proton-conducting membrane, which primary function is conducting the protons from the anode to the cathode, so it is important that the membrane is impermeable to the reactant gases, preventing the reactant crossover, and electrons, as referred before. The ion conduction in the electrolyte contributes to the losses, ohmic losses, in the cell voltage. Hence, one of the major tasks in fuel cell development is the reduction of these losses in the ionic circuit part, mainly related with the membrane thickness. On one hand, thinner membranes reduce the ionic losses, increasing the performance, but, on the other hand, the hydrogen crossover increases, and the lifetime decreases because it has more mechanical instability [16]. According to group [16], the optimum value of the membrane thickness achieved at 0.95 to 1.0 $A \cdot cm^{-2}$ (at 0.6 V) and 3000 and 5000 hours of life was 25 to 28 μm.

The most used membrane is Nafion® (Dupont), represented in Figure 3. Nafion® is produced by copolymerization of a perfluorinated vinyl ether comonomer with polytetrafluoroethylene (PTFE). The PTFE is sulfonated by the addition of a side chain ending of sulfonic acid HSO_3, called ionomer of the membrane because it is ionically bonded and so the end side chain is actually an SO_3^- ion. This ionomer is highly hydrophilic, so it attracts water, creating hydrophilic regions within a generally hydrophobic substance – the PTFE main chain. Nafion® is chemically resistant, mechanically strong, which allows the production of very thin films, acidic, which gives the ability to absorbing large quantities of water and, when well hydrated, is a very good proton conductor, making the most used material in PEM membranes. Companies as 3M, Gore, Solvay, Asahi and others make membranes with similar properties and characteristics.

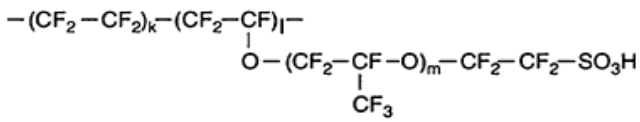

Figure 3. Chemical structure of Nafion®. Generalized formula with m = 1, l = 1, k = 5-7 [3].

Nafion® needs the presence of liquid water to provide a good proton conductivity. As the membrane adsorbs water, the first water molecules cause the sulfonated group to dissociate, forming hydronium (H_3O^+) ions. The water that hydrates the membrane then forms counterions that are localized on the sulfonated end groups, which act as nucleation sites. As more water

is added, the counterion clusters coalesce to form even larger clusters, until a continuous phase is formed with properties that approach those of bulk water [3]. The protons are relatively weakly attracted to the SO_3^- group and are able to move to the next sulfonic group [13, 17]. The hydration level is the number of absorbed water molecules per sulfonated group and it is represented by the parameter λ. For $\lambda = 0$, there is no water; to reach this point it would be necessary temperatures near the decomposition temperature of the polymer. Saturation occurs in Nafion® at $\lambda = 14$. One of the consequences of this strong coupling is that proton transport within the membrane is accompanied by the transport of water.

Due to the dependence of protonic conductivity with water content, it is necessary to ensure that the polymer electrolyte is safeguarded against localized drying. Indeed, a situation in which the membrane is in a "drying" mode of operation may lead to a catastrophic "death spiral" failure mode, since lower conductivity leads to higher resistances, increased localized temperatures and therefore an ever-increasing rate of drying, ultimately resulting in membrane failure. In real life operation, the constantly changing temperature and humidity conditions during the typical operation of a fuel cell lead to hygrothermal cycling loading of the membrane and directly affect its durability due to the development of significative mechanical stress with consequent formation of pinholes and cracks [18-20]. Polymer electrolyte membranes can degrade not only mechanically but also chemically through radical formation (OH and H) and side chain decomposition [21, 22].

2.3.2 Catalyst Layer (CL)

The catalyst layer is a porous structure containing a catalyst with high activity for anode and cathode reactions (HOR and ORR, respectively). There are two main groups of catalysts, the precious metal catalysts, containing Platinum (Pt) or Pt-alloys, supported on carbon particles and non-precious catalysts, nitrogen and carbon-based, containing iron, for example. The latter are still in the development phase and have no industrial relevance at this moment.

Most of catalyst layers in PEMFC are fabricated from a mixture of ionomer (for proton conduction) and nanoparticles of Pt or Pt-alloy catalyst supported on high surface area carbon (for electron conduction) that are all mixed together with a dispersion medium to form an ink-like random material. Usually the ionomer used is Nafion® because besides the proton conductivity to the catalyst sites, it is hydrophobic enough to prevent the pores from flooding. The Pt particles (3-5 nm) are supported on high surface area carbon particles, 20-30 nm, with a decreasing graphite nature toward the particle centre. These particles have the tendency to self-aggregate into agglomerates with sizes in the range of 50-100 nm of diameter [13]. This ink is then either sprayed, doctored, or jetted onto either a microporous layer on the gas diffusion media or applied directly to the polymer electrolyte. The nature and density of the

CL is determined by the nature of the ink, the interactions among its components, and the application process.

To ensure good performance, it is necessary to guarantee the three-phase boundary in each catalyst particle site, illustrated in Figure 4. This triple-phase is created by the reactant gases, electrons and protons where the reaction occurs. So, the Pt particle must be in direct contact with an electronic and ionic conductor, while allows the contact with the gas. As mentioned above, the ionic phase is provided by the Nafion® and the electronic phase by the carbon support particles. In this case, the optimal content of the ionomer is crucial. With insufficient ionomer content, some catalyst will be inaccessible, which results in low catalyst utilization and high ionic resistance, especially operating under dry conditions [23]. Excess of ionomer will decrease the porosity of the electrode, limiting the transport of reactants and products in and out of the catalyst layer [24].

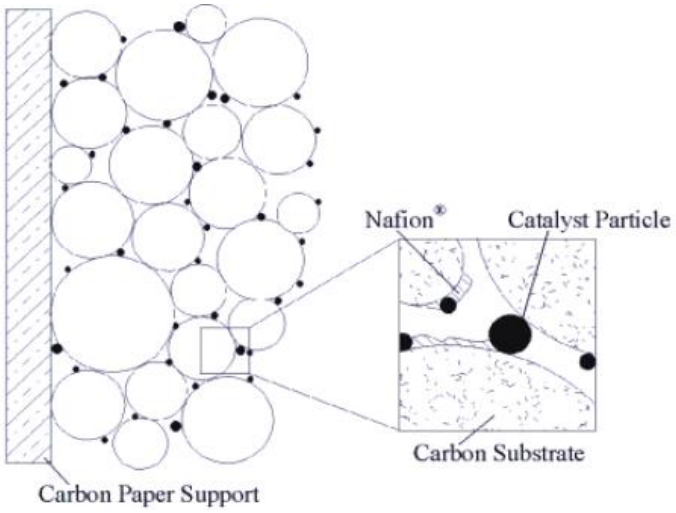

Figure 4. The three-phase boundary in the catalyst layer [9].

Due to the low temperature in PEMFC, the Pt loadings for the oxygen catalysts are significant to compensate for the slow reaction kinetics. Besides that, air is provided instead of pure oxygen for reasons of applicability, so the low partial pressure of oxygen leads to low activity. Performance targets for PEMFC electrodes are suggested to have a Pt loading of 0.125 $mg_{Pt} \cdot cm^{-2}$ (a total amount of 8 g_{Pt}) at each electrode to compare to the amount containing in internal combustion engines vehicles [13].

2.3.3 Gas Diffusion Layer (GDL)

The GDLs are responsible to distribute the reactant gases to the CLs, transport the water and heat generated in CLs to BPPs, to connect electrically between the CL and current collectors and to improve the mechanical stability of the MEA. In general, a GDL is constituted by a substrate of porous carbon fibres with thickness between 100 and 500 μm, and a thinner layer called microporous layer (MPL) just on one side (20-50 μm thick) and a hydrophobic agent,

usually PTFE. The porous layers are made of carbon paper or carbon cloth (electrically conductive) with a porosity between 90 and 70 % depending on manufacturer, type and compression level [25, 26]. Electron transport in GDLs occurs through the solid network of carbon fibres, while reactant and product gases as well as liquid water are transported through the void phase, or pore, of the GDLs. To aid liquid water removal from the cell and avoid flooding, GDLs are impregnated with PTFE or other hydrophobic materials. The MPL is commonly manufactured by intermixing a hydrophobic polymer, e.g. PTFE, with carbon black and is an important intermediate between the CL and GDL. The addition of MPLs reduce fuel cell ohmic resistance, increase fuel cell stability and enhance performance at high current density, especially under fully humidified conditions. The main functions of MPL are increasing the water removal rate [27], providing a better electrical contact [28], alleviating water accumulation by forcing the liquid water from cathode to anode [29], creating an in-plane diffusion pathway in the partially saturated layers [30] and improving the evaporation in the electrodes [30, 31]. One example of a hydrophobic treatment in GDL is by dipping the GDL into an aqueous PTFE suspension and then baking the treated GDL in an oven at 350-400 ºC to remove residual solvent and fix the PTFE particles into the GDL fibers. PTFE loadings can vary between 5-30 %, depending on the concentration of the aqueous PTFE suspension.

2.3.4 Bi-polar plates (BPPs) and flow fields

The two BPPs are located at the extremities of anode and cathode and they embody the flowfields. The BPPs distribute and separate the reactant gases, assist in the water management, are responsible for heat transport and current collection, and work as mechanical support for the thin and mechanically weak MEA. Since they need to be electrically conductive, they are made of either carbon-based materials (e.g. graphite composite) or metals (e.g. stainless steel) [32-34]. Graphite is conductive and has minimal corrosion in the fuel cell environment but requires additives for mechanical stability, are difficult to machine and are costly. The stainless steel is highly impermeable, highly conductive and have good mechanical properties, but has higher corrosion probability [35, 36]. Graphite plates are most commonly used in fuel cell hardware because metal plates suffer corrosion and dissolution under the high humidity and acidity conditions typical of PEMFCs [37-39]. To reduce the risk of degradation, metal plates are usually coated with thin corrosion-resistant films [39], which, however, add to the price of the final product.

As mentioned above, the flowfields are embodied in the BPP. Flowfield design aims to improve gas and charge transport to the catalyst site, removing excess liquid water from the channel and MEA, achieving appropriate compression and sealing and maintaining a uniform thermal profile. Depending on if it is a gas or a liquid, on the concentration of the reactant, different

flow field designs may be advantageous. In Figure 5, there is some comparative study about the different designs.

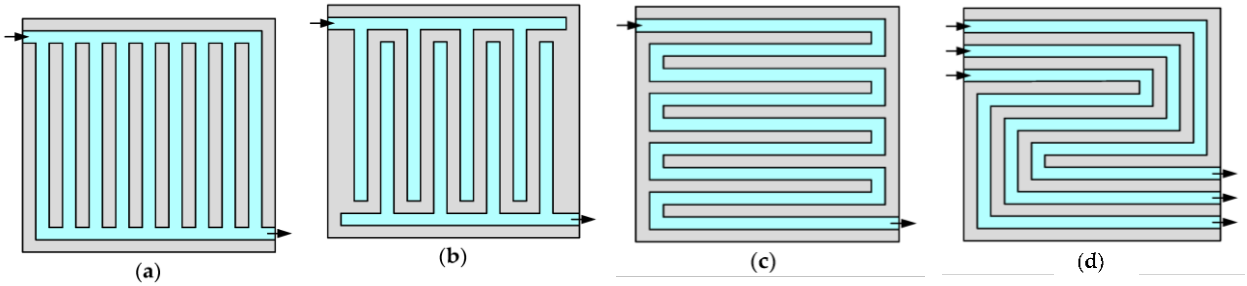

Figure 5. (a) parallel; (b) interdigitated; (c) single serpentine; (d) multiple (triple) serpentine.

In the parallel flowfield design (Figure 5a), the gas flow-field plate includes several separate parallel flow channels connected to the gas inlet and exhaust headers, which are parallel to the edges of the plate. Tests [40] indicates that these flowfield designs are prone to water blockage since reactant gases can easily by-pass blocked channels, so not allowing the necessary pressure to remove the liquid water blockage, so poor cell performance arises from the inadequate water drainage and poor gas flow distribution on the cathode side [40].

Interdigitated channels (Figure 5b) are another common design which incorporates dead-ended inlets and dead-ended outlets that are not connected, forcing the gas through the gas diffusion layer. This design can be advantageous especially at high current density operation due to the easily water removal from the electrode structure, preventing the water flooding. However, a large pressure loss occurs for the reactant gas flow, especially the oxidant air stream, higher than serpentine and parallel channels.

In single serpentine flowfield design channels (Figure 5c), the channels are generally linear and arranged parallel to one another but skewed to the edge of the plate. The flow channels on the anode and cathode plates are skewed in opposite directions to guarantee counter current flows. This design automatically drives the accumulated water droplets out of the cell by the pressure. However, there is a significant pressure drops and concentration gradients from the flow inlet to outlet created by the long reactant flow path with this channel layout.

The multiple serpentine flowfield (Figure 5d) is similar to single serpentine but consists in several continuous separate flow channels to limit the pressure drop. This design ensures adequate water removal by the gas flow through the channel, and no stagnant area formation at the cathode surface due to water accumulation. Multiple serpentine flow-field designs of this type reduce the reactant pressure drop relative to single serpentine designs, but the reactant flow path remains long enough to create relatively high pressure drops and concentration gradients in each the serpentines.

2.3.5 Cell assembly

In practice, all MEA components are manually prepared in laboratory, so it takes some hours do prepare and assemble all PEMFC components. Besides that, the assembly of the MEA with the bi-polar plates need to be careful to ensure a good contact between all components. In addition to the alignment of the components and avoidance of contamination particles, for example, the thickness and compressibility needs to fit all other components, and the clamping force needs to be adjusted. Otherwise, it will compromise the fuel cell performance and allow reactant leakages. In particular, each novel cell, with any newly developed component, may require adjustments in the sealing concept. In Figure 6 is shown a typical PEMFC assembly.

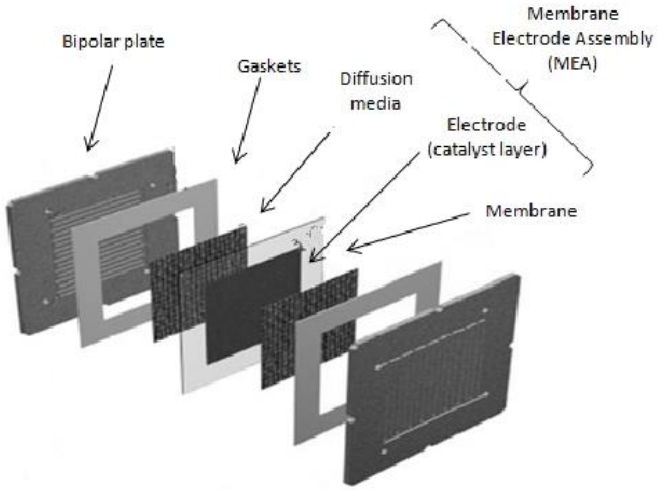

Figure 6. PEMFC components assembly [13].

2.4 Water management

Water management in the membrane is one of the major issues in PEM technology. The water content in the PEMFC is influenced by electro-osmotic drag, back-diffusion, water producing by ORR (equation 2) and external humidification of the reactant gases. A scheme of water balance mechanisms in PEMFC is represented in Figure 7.

The electro-osmotic drag transports water from anode to cathode, in which protons migrate through the membrane drag along water. Back-diffusion is created by the different water content; with more water in the cathode, the water will move from the cathode to the anode. The external humidification of the reactant gases is provided by adding water content to the feed gases, at a given temperature, which will influence the relative humidity of the gases. The electro-osmotic drag and the water producing by ORR are directly proportional to the current density while the back-diffusion depends on the thickness of membrane and the relative humidity (RH). Since the back-diffusion occurs at much slower rate than the electro-osmotic drag, and water is produced in cathode side, water will accumulate at cathode. So, it is necessary a constant remove of the water in the cathode.

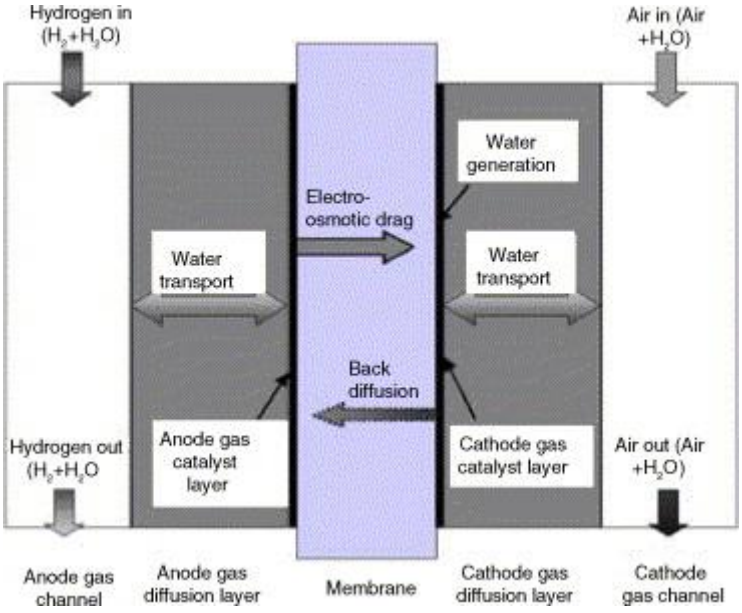

Figure 7. Water transport mechanisms through PEMFC [41].

The water balance in the cathode is crucial for the performance of the cell. A large number of models have been proposed in the fuel cell literature during the past decades to study water management and based on these studies, it was identified that the key to appropriate fuel cell water management is to strike a balance between membrane dehydration and water accumulation (flooding) in the cathode. As stated before, the membrane needs to be sufficiently hydrated to maintain good ionic conductivity and reduce ohmic losses, usually provide by humidification of reactant gases. When the cell is operating with dry gases, the membrane and ionomer phase of the electrode may dry out, leading to a rapid decline of the power density. On the other hand, under high relative humidity and high current density operation, removing the excess water generated in the electrodes is critical to avoid water accumulation and achieve high performance, preventing the flooding in the pores.

The water accumulates at the cathode catalyst layer not only from reaction product water but also from the electro-osmotic drag. There are two possible directions to remove this accumulated water. First, water will be transported through the cathode gas diffusion medium to the air gas channel either as vapor or in the liquid form. Second, there will be back-transport of water through the membrane and the anode gas diffusion layer to the fuel gas channel. The respective rates at which these processes take place depend on the driving force for the water transport in either direction or due to the permeability of the components to water [42]. The permeability to water of the components is also important. For example, thin membranes allow for fast water transport to the anode, reducing flooding at the cathode. In thin membranes, the back-transport of water can often overcompensate the water transport that is associated with the electroosmotic drag, thus preventing drying out at the anode.

Nowadays, more than ever, the MEA materials are prepared to remove more efficiently the liquid water accumulated. The gas diffusion media are hydrophobized to such an extent that they allow transport of liquid water, an important mechanism at near-saturated conditions, as well as of water vapor and reactant gases. An important role is played by the MPL. Because of the presence of small hydrophobic pores, a substantial liquid water capillary pressure can be built up, enabling a good gradient in the chemical potential of water to drier sections [29]. The optimization of gas diffusion media and the application of the MPL have led to significant improvement of the fuel cell performance at saturated conditions, showing their critical role.

2.5 Characterization of condensed water at the flowfields (Thermography)

As mentioned in section 2.4, water management is one of the major topics in PEMFC, so over the last few decades different methods have been developed to characterize the condensed water at the flowfields such as thermography, neutron radiography [43], X-ray [44], synchrotron X-ray [45], magnetic resonance imaging [46], among others. This work focuses on infrared (IR) thermography method.

In its definition, IR thermography is a technique used for detecting and measuring variations in the heat emitted in the form of infrared radiation by various regions of a material and transforming them into visible signals that can be recorded photographically. To better understand this method, it will be further explained the electromagnetic spectrum (especially infrared radiation) and the blackbody radiation.

2.5.1 Electromagnetic Spectrum and Infrared radiation

Electromagnetic radiation is a way of energy propagation through a vacuum or a material medium without mass transport and has different characteristics depending on its wavelength and frequency. Regarding the body, the electromagnetic spectrum is all the electromagnetic radiation that is emitted or absorbed and extends from the radiation of lower energy such as radio waves, microwaves, infrared (IR) waves or visible light to electromagnetic radiation with higher energy such ultraviolet, X rays and gamma rays.

The electromagnetic spectrum is divided into several wavelength intervals and extends from very small wavelength values to extremely large ones. In Figure 8 the electromagnetic spectrum is represented along with IR and visible radiation range.

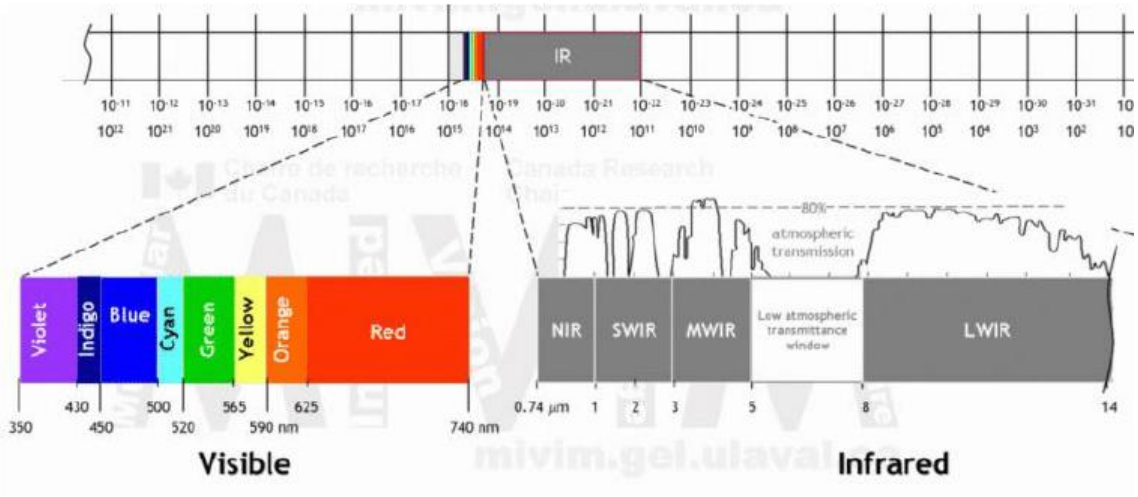

Figure 8. Electromagnetic spectrum with visible and infrared wavelength intervals [47].

The heat is transferred by the absorption of the radiation. Thermal radiation region embraces the entire IR and visible bands as well as the upper part of the ultraviolet band, so it is possible stablish a relation between IR radiation and temperature. IR wavelength range is from 760 nm to 1 mm and it is subdivided into four smaller bands: near IR (0.76-3 μm), middle IR (3-6 μm), far or long IR (6-15 μm) and extreme IR (15-1000 μm) [48]. All bodies that present a temperature above absolute zero (0 K) emit IR radiation [49, 50]. For example, a PEMFC operating at 80º C will emit most of its radiation in the far IR range.

2.5.2 Blackbody Radiation

A blackbody absorbs all the incident radiation, independently of the wavelength and the direction of the radiation. For a specific temperature and wavelength, there is no surface that can emit more energy than a black body. The emitted radiation of a blackbody depends on the wavelength [51]. So, the spectral black body emissive power depends on the wavelength and is possible to plot in the graphic for several absolute temperature values as it shown in Figure 9. In this plot, for each wavelength, the emitted radiation increases significantly with temperature and the different curves never cross each other. Each isothermal curve tends to zero for both very large and very small value of wavelength, having a maximum at some intermediate wavelength.

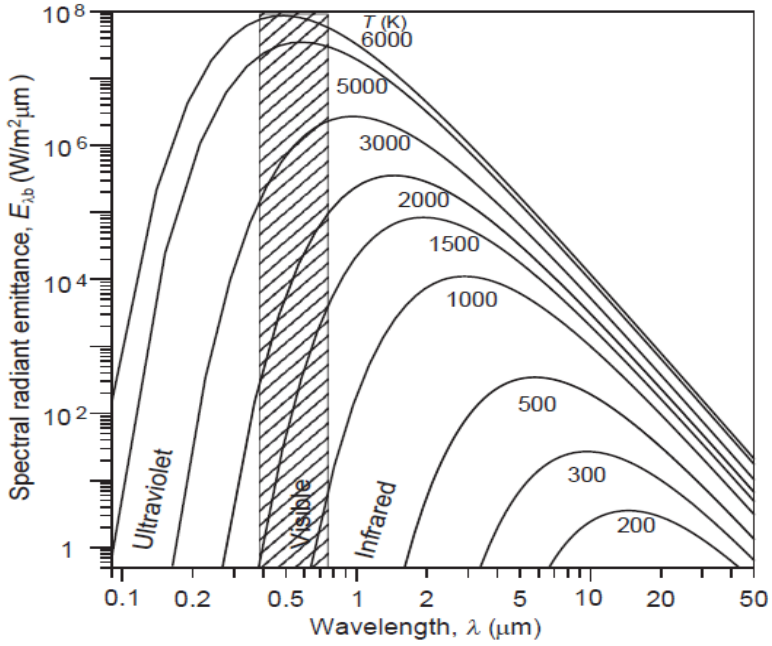

Figure 9. Blackbody emissive power curves (Planck's law) [52].

The quantity characterizing the emission of electromagnetic radiation by a body is called the total emissive power, *E*, that is the energy emitted by a unit of time and surface. The total emissive power is not equal in all wavelengths, so there is also the spectral emissive power, E_λ, which is the energy emitted by a unit of surface, time and range of wavelength, represented by Equation (7).

$$E_\lambda = \frac{2\pi hc^2}{\lambda^5\left(e^{\frac{hc}{\lambda kT}}-1\right)} \tag{7}$$

where *h* is Planck's constant (h = 6.6x10^{-34} J·s), *c* is the speed of light, λ is the wavelength of the radiation being considered, *k* is the Boltzmann's constant (k = 1.38x10^{-23} J·K^{-1}) and *T* is the absolute temperature of the blackbody (K).

Stefan-Boltzmann's Law expresses that the total emissive power of radiated energy from a blackbody is proportional to the fourth power of its absolute temperature, represented by Equation (8), which mean that small changes in temperature results in big changes in the emissive power. This law can be obtained by integrating Planck's Law over the entire spectrum.

$$E = \sigma \times T^4 \tag{8}$$

where σ is the Stefan-Boltzmann constant (σ = 5.67X10^{-8} W·m^{-2}·K^{-4}). This relation is important to explain how the calculation of the temperature from the emissive power is very sensitive and allows differentiation of areas at different temperatures, as they will have different emissive powers. For real bodies is added the emissivity to the equation above, represented in Equation (9):

$$E = e \times \sigma \times T^4 \tag{9}$$

where *e* is the emissivity and varies in the range [0,1] (for blackbodies the emissivity is 1).

Differentiating the Planck's law with respect to λ, it is possible to obtain the wavelength which reaches the maximum radiation intensity, λ_{max}, using the Wien's displacement law, represented in the Equation (9).

$$\lambda_{máx} = \frac{d_w}{T} \tag{9}$$

where d_w is Wien's displacement constant ($d_w \approx 2898$ μm·K). This equation practically states that at PEMFC operating temperature of 80 ºC (353 K), the radiation peak lies in the far IR at about 8.2 μm, the value that can be important for IR cameras. The sun radiation peaks at about 0.5 μm in the visible light spectrum.

2.6 Optical system

The IR optical system is very similar to typical visible optical systems. The main difference between them consists of the material that constitutes the optical components, which has to be transparent in the used IR band. Most of the optical glasses that are transparent in the visible band normally appear opaque in IR bands, so particular materials must be used for IR lens manufacture. There are also differences between materials used in the 3-5 μm (middle wavelength IR - MWIR) or the 8-12 μm (long wavelength IR – LWIR) band. Typical optical materials used for MWIR and LWIR are Germanium, Zinc Selenide, Zinc Sulphide, Sodium Chloride, Potassium Bromide. Except for Germanium, all other materials are transparent also to visible light [48]. IR cameras lenses are primarily made of Silicon for the MWIR band and of Germanium for the LWIR one. Even if transparent in the MWIR band, Germanium is seldom used there as it is rather expensive.

An important parameter for evaluation of the lens system is the material refractive index, *n*, which is represented in Equation (10). Large values of *n* enable a large deviation of the incident radiation and, thus, a smaller number of optical elements are needed to construct a diffraction-limited lens. However, a large refractive index produces a large reflectivity coefficient and a relatively small overall transmittance.

$$n = \frac{velocity\ in\ vacuum}{velocity\ in\ medium} \tag{10}$$

With the refractive index value, it is possible to determine the material transmissivity, τ, as shown in Equation (11).

$$\tau = \frac{2n}{n^2+1} \tag{11}$$

For Germanium, the refractive index is near 4 in the MWIR and LWIR bands and applying the equation 11, the normal transmissivity coefficient is around 0.47, which is low value, leading

to the need of applying an anti-reflective coating. In Figure 10 is plotted the transmittance percentage in MWIR for a 2 mm thick germanium slab with and without the triple-layer antireflection coating. It is shown clearly that the transmittance increases significantly for the antireflective coating.

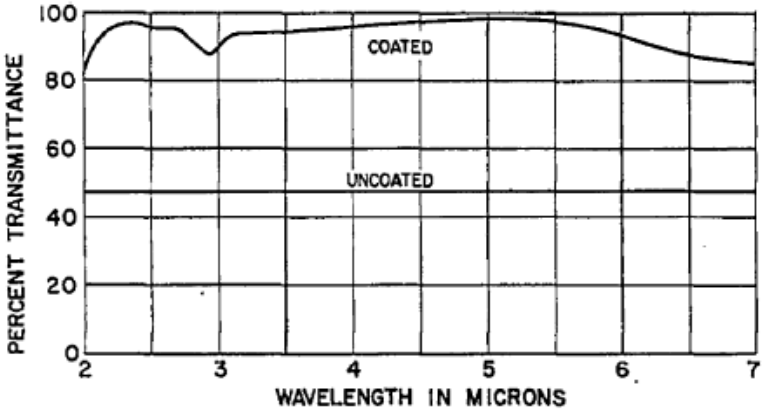

Figure 10. Transmittance of a 2mm thick germanium slab with and without antireflection coating [48].

Infrared thermography includes also an IR detecting device to sense the thermal energy that is radiated from objects in the IR band, and then is transformed into a video signal by some specific software and basic relationships, and finally, into the object surface temperature map.

There are specific cameras to view specific wavelengths [51]. Most of the currently used IR camera temperature detectors are sensitive in either the middle or the long-wavelength spectral bands, though the band between 5 and 7.5 μm is seldom used because of its rather high atmospheric absorption. There are also detectors available in the near-infrared band and in the extreme infrared band, but they are used much less for standard thermo-fluid-dynamic [48]. The most common detector array types used on commercial IR cameras are microbolometers, for the handheld and automation models, and quantum sensors, for high-performance applications [52].

An IR imaging device should be considered as a precious ally to consult for diagnostics and preventive purposes, for the understanding of complex fluid dynamics phenomena or for material characterization and procedures assessment, which can help improve design and fabrication of products [52]. For the particular case of PEMFC, it could help the understanding of water management and the producing of liquid water, and after this understanding, it could be changed some material characteristics or design to improve the performance by avoiding the flooding, for example.

3 Setup

3.1 Fuel Cell, Test-bench and Operation

In order to develop the thermography technique along with PEMFC and observe directly inside the fuel cell through an infrared window, a modified fuel cell design was required comparing to a conventional one. The design modifications were applied on cathode while the anode remains like the conventional one. The cell development and operation in this work can be divided into the following sub-sections further described: MEA, Anode, Cathode, Sealings, Assembly, Test-bench and Software and Operation.

3.1.1 MEA

The MEA consists of CCM (catalyst coated membrane) and GDLs (SGL Carbon Sigratec 25BC), as explained on chapter 2 (Figure 6), where the gaskets used were commercial polyolefine based (IceCube™, Freudenberg SE) gaskets placed on both sides of the membrane to seal the reactants and products, observed in Figure 11. A 6 x 6 cm square membrane coated with the catalyst was cut to ensure that the whole active area is covered by the membrane. For GDL, it was cut a 5 x 5 cm square, and it was placed with the MPL facing the membrane, and the graphitic carbon to the outside, to provide contact with the cathode and anode flowfields. Around MEA it was placed an extra gasket to avoid a short-circuit (see Appendix, Figure A.4. – Bottom middle).

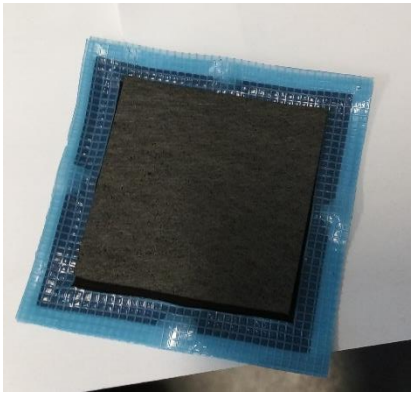

Figure 11. MEA Assembly with two IceCube gaskets.

3.1.2 Anode: bi-polar plate

The anode bi-polar plate is a stainless-steel plate coated with gold (made by DLR) and it had a single serpentine flowfield embodied, so it worked as an endplate, current collector and flowfield in one single material. As it is illustrated in Appendix, Figure A.1, a PTFE gasket was placed around the flowfield, to avoid any gas leakage.

3.1.3 Cathode: bi-polar plate and flowfield

The cathode suffered several modifications. To embody the infrared window in the centre of the cathode BPP, the flowfield must be removed and incorporated in a separate material so, in this case, the flowfield worked has a current collector as well. The bi-polar plate is made of stainless steel and his new design is specified in Figure 12.

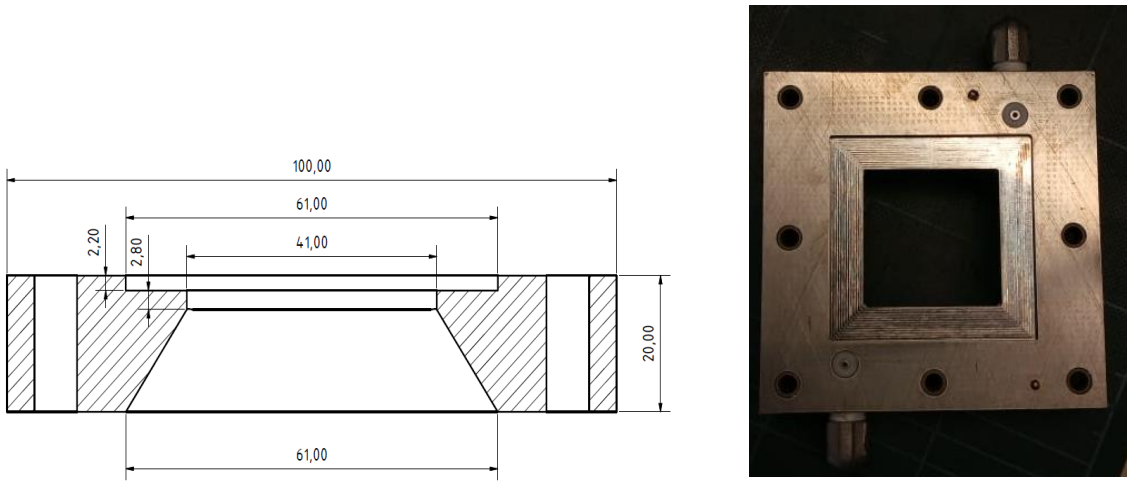

Figure 12. Cathode bi-polar plane new design to incorporate the infrared window.

As it is shown in Figure 12, it was a 10x10 cm stainless steel BPP with 2 cm thickness. The bi-polar plate was cut with a 6x6 cm portion with 2.20 mm depth where the window was placed. The infrared camera was placed on the opposite side, with a maximum visualization window of 4 x 4 cm. On inlet and outlet of the BPP, 2 PTFE o-rings are placed to avoid the air leakage. The windows placed have 6 x 6 cm and thickness of 2010 ± 30 µm. During this work two different window materials were used, quartz and germanium, that will be mentioned further in section 3.2.2.

The separated flowfield plate of 10x20 cm and 1 mm thickness is made of stainless steel too with a single serpentine design (as in anode flowfield), represented in Figure 13.

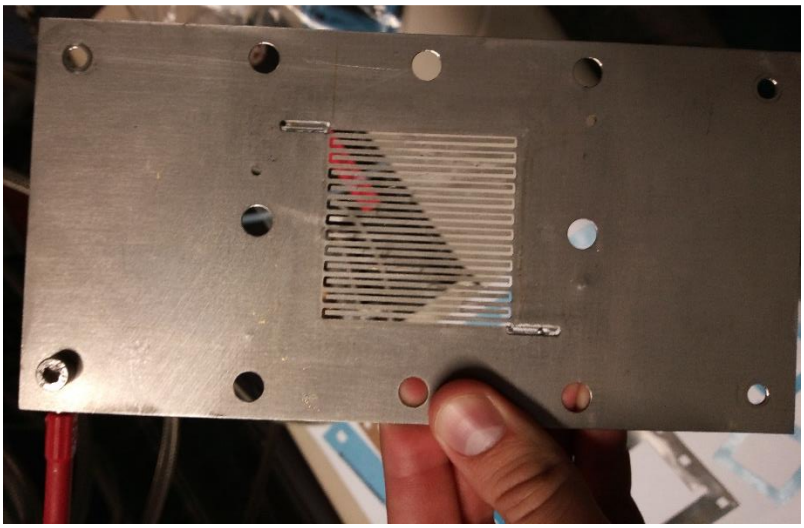

Figure 13. Separated flowfield plate with single serpentine design.

Between the flowfield and the BPP and between the window and BPP it was necessary to place sealings to avoid possible leakages. From now on, to simplify the language, the sealing between the cathode flowfield and the cathode BPP is referred to as cathode flowfield sealing and the sealing between the window and the cathode BPP is referred as window sealing. Different sealing materials with different thicknesses were studied to better understand which material(s) was the best solution to this setup. In chapter 4 it is explained with more details the possibilities under study.

3.1.4 Assembly

Although the design of the cell is different, the components are assembled in similar positions as in the traditional assembly (Figure 7), illustrated in Figure 14. After the components are placed as stated, the cell is sealed with 8 screws by a diagonal torque followed by cross torque with small increments. Along with the work, different torque values were applied, varying between 2.0 and 3.5 N·m. Between 0 and 2.0 N·m it is applied increments of 0.5 N·m and, after 2.0 N·m, smaller increments of 0.2 N·m. These small increments are crucial to minimizing the unbalanced tensions created on quartz or germanium windows, ensuring the stability of the window.

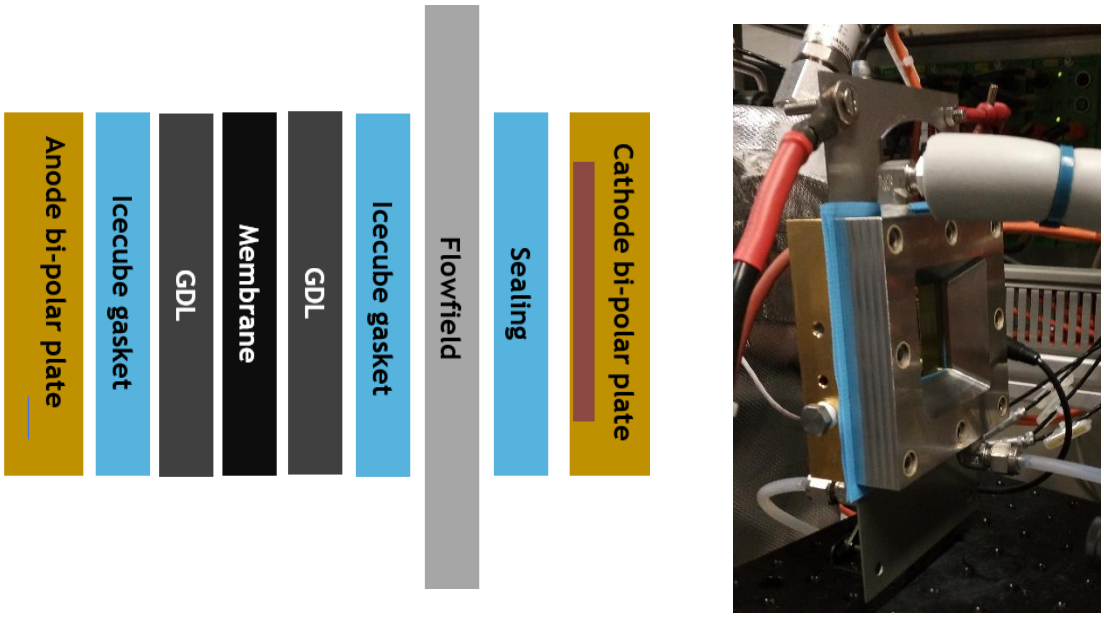

Figure 14. Fuel cell assembly (scheme and real image, respectively).

3.1.5 Test Bench and Software

The fuel cell assembled was then operated in the test bench, illustrated in Figure 15. The reactant gases were supplied to the bottom of each bubbler (place at anode and cathode side) to establish the desired relative humidity before reaching the cell. The operating temperature was obtained by a heater placed in the anode (due to new cathode design, it was impossible to place any heater on it) and controlled by a temperature sensor in anode too. The current collectors were placed in anode BPP and cathode flowfield. All parameters used to perform the tests were controlled individually, using an inhouse Simatic WinCC based software. Under the cell, an optical board was placed where the optical system was installed (explained in detail in sections further). The optical system was connected to an independent computer with an independent software, also developed in-house.

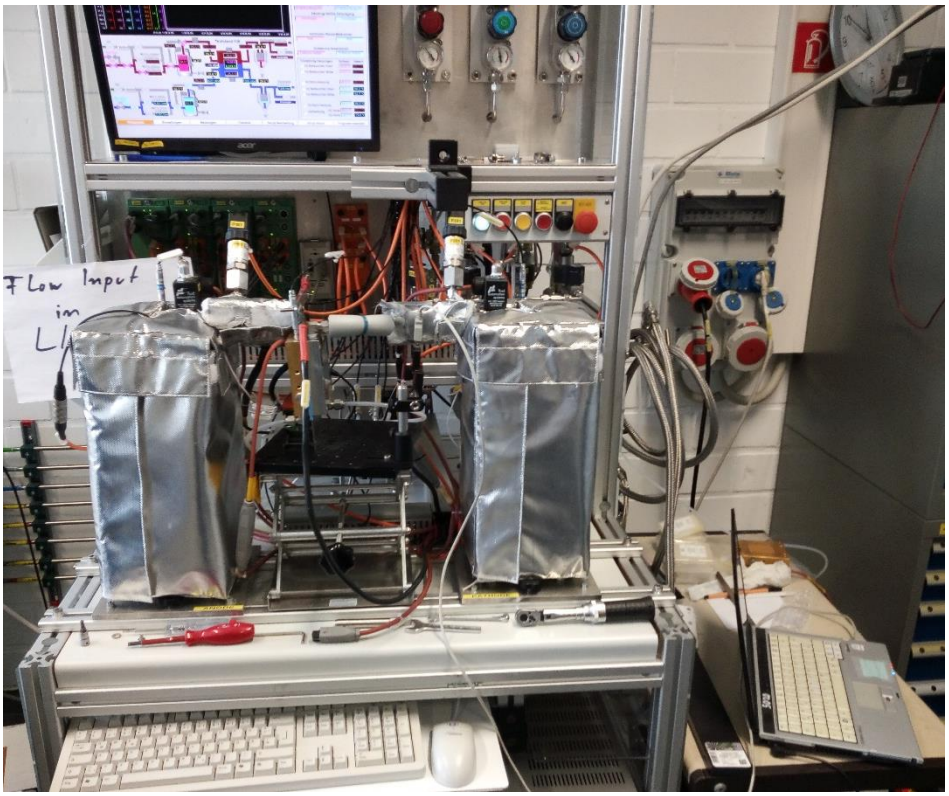

Figure 15. Test-bench overview.

3.1.6 Operation

Prior to the tests, the MEA need to perform a pre-conditioning or activation conditioning. The operation conditions for pre-conditioning are discriminated in Table 1. In further tests, different operation conditions were applied (more detailed in chapter 4).

Table 1. Standard operation parameters for pre-conditioning.

Parameters	Value	Unit
Cell operating temperature	80	ºC
Gas inlet temperature (anode/cathode)	85/85	ºC
Gas inlet humidity (anode/cathode)	50/30	%
Flow stoichiometry (anode/cathode)	1.3/1.5	-
Inlet pressure (anode/cathode)	1.5/1.5	bar

3.2 Optical System

The optical system used to develop this work is composed of an infrared camera, window frames and lens.

3.2.1 Infrared camera

In this work, the IR camera used was a Seek Thermal CompactPRO, designed and developed for smartphones, iPhone® and Android™, with the purpose of expanding the capabilities of smartphones to a thermal imaging tool. It is possible to run the IR camera, recording images and videos directly to the smartphone and easily share them with a free app called "Seek Thermal", available in Apple and Google Stores. The actual price is $ 499 [53]. The main applications proposed by the brand are to inspect mechanical and electrical equipment, monitor hazardous environments from a safe distance, roof, insulation and HVAC systems inspection, among others, which makes it a good solution for general thermal inspection. For this work was required a more close-up study, so perhaps this IR camera was not the perfect solution. Nevertheless, for a low-cost thermography study, the camera was one of the best solutions in the market. Figure 16 provides a quick look to the camera itself and the camera app in use on a smartphone. Table 2 schemes some of the technical specifications of the camera.

Figure 16. Seek Thermal app with camera conection and Seek Thermal CompactPRO, respectively [53].

Table 2. Camera technical specifications.

Specifications	Description
Thermal sensor (pixels)	320 x 240 (76 800)
Detection Distance (m)	0.15 - 550
Field of view (degree)	32
Temperature Range (°C)	-40 - 330
Lens Material	Chalcogenide

Microbolometer	Vanadium Oxide
Thermal Sensivity (mK)	< 70
Spectral Range (µm)	7.5 - 14

3.2.2 Window Frames

As mentioned in the previous section, throughout this work it was used 2 windows from different materials: I) quartz and II) germanium illustrated in Figure 17.

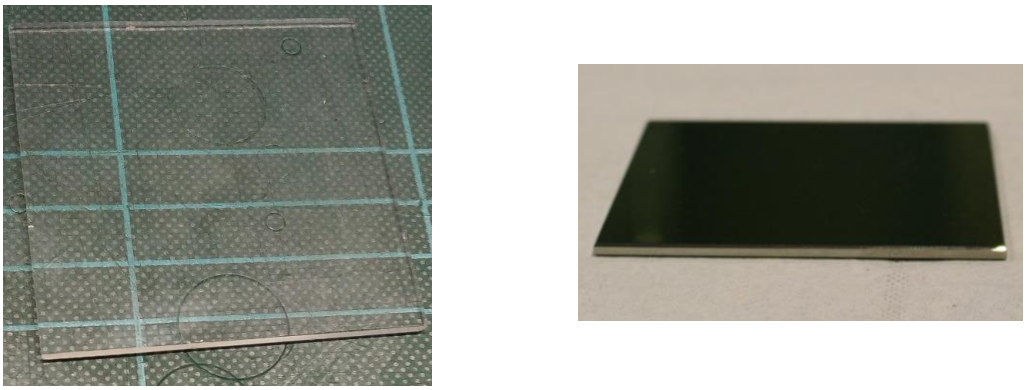

Figure 17. Quartz (on the left) and Germanium (on the right) window frame with 2 mm thickness.

I) Quartz

Quartz is a silicon dioxide (SiO_2) mineral and is the most abundant mineral on Earth as a component in most rock types with unique properties make it one of the most useful natural substances [54]. Among many possible applications, a quartz glass frame is an interesting option as a window in the fuel cell at first assembly trials. Quartz is an undesirable material for thermography experiments performed in this work because it is a material transparent to visible radiation and opaque to infrared radiation (transmittance plot in Appendix, Figure A.2.). However, it is a more stable and cheaper material compared with Germanium. With the same dimensions, it is a good material to make the transition between a conventional cell assembly and the new design cell developed in this work for the costly antireflective coated germanium window. The quartz relevant properties for this work are summarized in Appendix, Table A.1.

II) Germanium

Pure germanium (Ge) is a hard, lustrous, grey-white, brittle metalloid, has a diamond-like crystalline structure and it is similar in chemical and physical properties to silicon. It is an important semiconductor, mainly used in transistors and integrated circuits. In optics, Ge is a material that blocks UV and visible wavelengths but allows the transmission of IR from 2 µm. The high refractive index and low optical dispersion make germanium desirable in optical systems (for example, lens or window design). It transmits over 45% between 2 and 14 µm and

its transmission degrades slowly at 100 ºC and then more quickly above 200 ºC, which is perfect to operate within the PEMFC. Typical optical applications for germanium include FLIR (Forward Looking Infrared) and FTIR (Fourier Transformed Infrared) spectroscopy systems, alongside other analytical instruments [55]. Since germanium has transmission lower than 50% and, according to Korth Kristalle, it has a reflective loss of 36.04% at 10 µm [56], a coating must be applied with anti-reflection agents. The most indicated anti-reflective coating is a diamond-like carbon with refractive index 2.0, especially used in thermal imaging cameras with a wavelength range of 8-14 µm. The germanium anti-reflective coating used in the present work was supplied by II-VI GmbH. Figure 18 shows transmittance values when applied the anti-reflective coating, providing a considerable improvement. The germanium relevant properties for this work are summarized in Appendix, Table A.2.

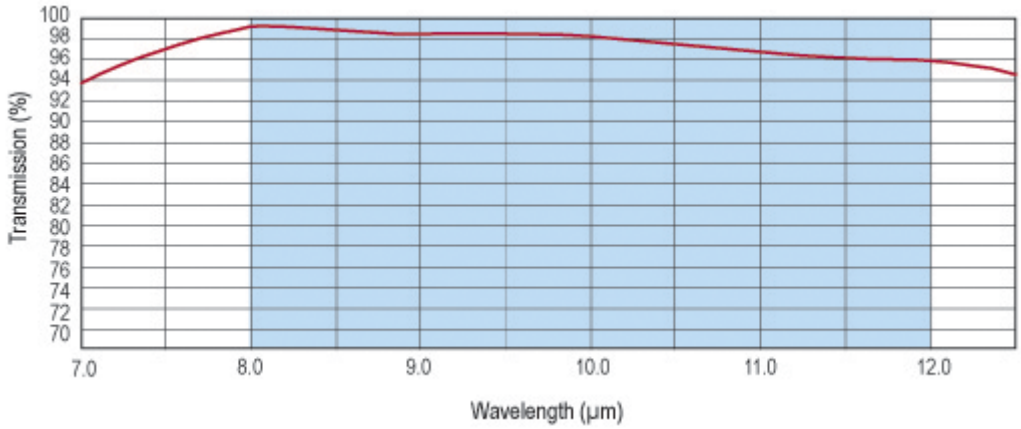

Figure 18. Germanium transmission curve with anti-reflective coating.

3.2.3 Germanium Lens

A non-coated germanium lens was used to achieve a considerable magnification of the ribs and channels inside the cell. With the help of a 3D printed polymer support, the lens was placed in the camera as shown in Appendix, Figure A.2. This germanium lens is a positive meniscus shaped with one spherical and one flat surface. In general, without the anti-reflecting coating, the transmittance is worse than with anti-reflecting coating. In this work, the purpose was to achieve a magnified image, to demonstrate the benefits of the anti-reflective coated germanium window.

4 Results and discussion

As mentioned in Chapter 3, a new cathode was designed with new materials to implement the window for camera visualization by infrared radiation. Some of these components remain the same during this work such as the anode bi-polar plate, the MEA components, the ice cube gasket surrounding the MEA (between the anode BPP and cathode flowfield frame), the cathode flowfield and the cathode bi-polar plate. The other materials and torque and operation conditions differed from test to test.

Throughout this chapter, in further testes, current values obtained at potential values between 0.6 and 0.5 V were commonly referred to as criteria.

4.1 Fuel cell operation with window

First, it was necessary to prove that this new fuel cell concept works. In order to accomplish this, first trials were made with quartz window instead of directly using the germanium window with anti-reflective coating for two reasons: the germanium window is more fragile than the quartz window, and much more expensive. So, to perform the first assembly tests and apply a considerable torque, it was safer to use the quartz window.

The fuel cell assembly was constituted by the components stated above, the quartz window frame, one IceCube gasket in the cathode flowfield, with 350 µm thickness, and another IceCube gasket with the same thickness in the window. Before assembly, the thickness of the quartz window was measured in the four corners to confirm that the thickness along the window was uniform. The values for the four corners were 2.000, 2.000, 2.000 and 1.999 mm, demonstrating a uniform thickness. The cell was operated at the pre-conditioning conditions (referred in section 3.1.6) and assembled with a 3.0 N·m torque. The cell operates successfully, and it was possible to register a polarization curve. The polarization curve was recorded in galvanostatic mode. The measurement started with a current density of 0.50 $A \cdot cm^{-2}$ with increments of 0.05 until 0.80 $A \cdot cm^{-2}$ and after this value, in increments of 0.10 $A \cdot cm^{-2}$ until reaching the current density value where the potential observed were close to 0.25 V. Once recorded a potential value close to 0.25 V, to avoid any membrane damage due to high current densities, the current density values were decreased in the reverse way until 0 $A \cdot cm^{-2}$.

Figure 19 compares two polarization curves, one from a conventional cell and other with the cell with the quartz window, demonstrating that this cell concept worked. Observing the comparison between the two curves, it is also possible to conclude that the performance is lower when implemented the window, what was expected because more components were added that hinder good contact between all cell materials when assembled.

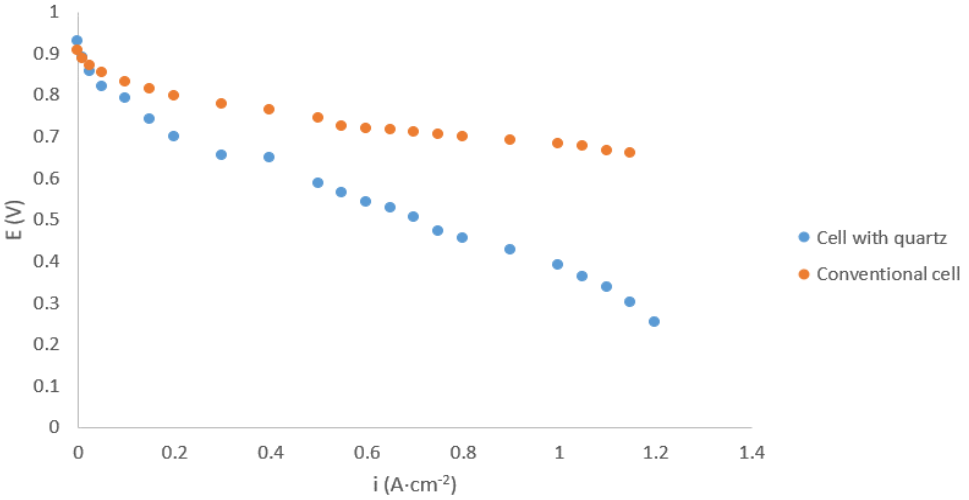

Figure 19. Polarization curves with conventional cell and cell with quartz window incorporated.

4.2 Integration of the Infrared transparent window

Once performed the cell with quartz window incorporated, the first attempts with the germanium window started. Considering the fragility of the germanium window and the diminutive practical knowledge about this material handling, a more conservative approach was required. At first, as well as in the quartz window, it was measured the thickness of the four corners of the germanium window, with the values of 2.030, 2.030, 2.030 and 2.030 mm. Then the cell was assembled with less torque, started with 2.2 N·m and increasing to 2.5 N·m (already considered a reasonable torque to assemble a fuel cell), and the current density values obtained in the 0.6-0.5 V range was around 0.1 and 0.2 A·cm^{-2}, values that were far below expectations.

4.2.1 Sealings

Consequently, different approaches to sealings composed of other materials and with different thicknesses were studied and tested to understand the better sealing option for a not perfect but satisfactory cell tightness. The sealing material used was IceCube gaskets, a polyolefin elastomer (35 FC-PO 100) supplied by Freudenberg (SE); Viton®, synthetic rubber and fluoropolymer elastomer produced by DuPont (at the top middle in Appendix, Figure A.3.); polytetrafluoroethylene, PTFE with fiberglass (at bottom right in Appendix, Figure A.3.). Table 3 presents the sealing thickness if the material is compressible or not, and where they were incorporate in the cell (flowfield or window) in the further gases pressure tests.

Table 3. Summary of sealing materials.

Sealing Material	Thickness (µm)	Compressible	Flowfield - BPP	Window - BPP
Ice cube gasket	350	✓	✓	✓

Ice cube gasket	500	✓	✓	✓
PTFE with fiberglass	220	×	✓	×
Viton	474	×	✓	×

The tests consist of bringing in the reactant gases at a constant flow rate (for example, the flow rates used in the pre-conditioning tests) without heating the whole system, setting the outlet pressure at anode and cathode to 2.00 bar and checking the real outlet pressure measured for the different sealing options considered in the cathode flowfield and the window, for different torques. The difference between established pressure and outlet pressure measured is the pressure drop originated by flow resistance and the lack of tightness between the cell components for the options taking into account, schemed in Appendix, Table A.2. It is important to mention that before any test, a conventional cell was assembled, and it was ensured that the established and the real pressure were not deviating strongly, which means no leakage reported. It should be noted that it was safer to work and to perform with compressible sealings (ice cube gaskets) in the window to avoid breaking it.

According to Table A.2. (Appendix), no combination of sealings reached close to the set-point outlet pressure of 2.0 bar, which mean that the gases will leak regardless the option considered. Besides that, it was confirmed that the option tried in previous tests with quartz and germanium window was the best option, alongside the option 3 (one 500 µm ice cube gasket in the window and another with same thickness in the flowfield).

4.2.2 Silicone

As compressible sealings demonstrated better results, the possibility of producing silicone sealings of a desired thickness was studied. The silicone was prepared in the laboratory and it is composed of a base compound and a catalyst. The base used was XIAMETER® RTV-3110 Base, which consists of a pourable rubber that becomes firm, flexible silicone rubber when cured. To be cured, the catalyst used was XIAMETER RTV®-3010-S. Appendix, Table A.3. indicates the approximate working time and curing time according to the Base/Catalyst mixing ratio by weight.

The Base/Catalyst weight ratio used during the following testes were 10:1, which means 2 hours of working time and 7 hours of curing time. After mixing the base and the catalyst, two different approaches were tried. In one, the silicone was placed in a syringe and applied directly in the cathode bi-polar plate with a needle and then the flowfield cathode plate was just placed on top of the bi-polar plate and left to cure. On the other, two smooth aluminium plates were

used as mold. To ensure that the sealing silicone remains at a homogeneous thickness, several metal washers with 600 µm total thickness on one of the aluminium plates. Posteriorly, the silicone was deposited on top of the plate and the other plate was placed on top of silicon and left to cure.

None of these approaches achieved any satisfactory result. The first approach, when applied the torque of 3.0 N·m, it provoked the window (germanium one) to break. The amount of silicone placed with the syringe was not enough to guarantee a sufficient thickness when the cell was assembled and compressed, increasing tensions in the window until fracture. Besides that, the silicon was manually placed with the syringe, which means that probably the amount placed around the bi-polar plate was not uniform, causing even more stress and unbalanced stress in the window. However, if too much silicone would be placed, it could spread through the flowfield and block the fluid transport. For the second approach, it was difficult to guarantee the homogeneity of the silicone layer.

The silicone approach was considered advantageous because it is possible to produce principally any desired thickness in a laboratory, suitable tools given to set the distance, and it is a very compressible material. It could be an interesting way if applied with more sophisticated techniques, to guarantee exactly the thickness desired. It proved, however not a suitable method to solve this specific sealing problem.

The silicone attempt was not as projected, making the ice cube gasket the best material among all other materials studied. So, several testes were tried with the germanium window and the ice cube sealings, progressing the torque from 2.5 (last torque value before the other sealing attempts) until 3.0 N·m (torque value used in the initial cell operation with the quartz window, operation with satisfactory performances). Except for the exchange of the quartz window for the germanium one, the tests were developed until the point that it was applied the same conditions as used initially to operate the cell with the quartz window, i.e., 350 µm thickness ice cube gasket in the window and the cathode flowfield, with a 3.0 N·m torque. As the results still were not as desired, the entire cell was checked for reasons for the sealing deficiency. As structural defects of the sealing material and the cell components, e.g. deep scratches, could be ruled out, the flatness of the cathode flowfield was found to be compromised. A fresh, straight edged steel ruler was used to check the flatness of the different cell materials. When the cathode flowfield plate flatness was measured a bend was detected. Since the material bending at this point was even visible to the eye (Figure A.5), it was certainly a significant curvature, and turned out surprising, as it was not obvious during the first experiments.

4.2.3 Identification of a design fault

After detecting the material curvature, it was necessary to quantify this bending. It was measured with the steel ruler and steel sheets of different, defined thicknesses. The ruler was

placed in the flowfield plate and then it was tried to pass through the steel sheet: if it passed, it would have at least that thickness; if did not pass, it would not reach that thickness. This simple procedure allowed to quantify, in a rough way, the curvature. Without the cell assembly, the height of the reached values between 150 and 200 µm; with the cell assembly with 2.5 N·m torque, it could be reduced to values between 50 and 60 µm; with the cell assembly with 3.7 N·m torque, values between 40 and 50 µm. These values demonstrated that with assembly it was possible to decrease part of the bend, but not entirely, making this defect critical to assembly the cell in a proper way, ensuring a good contact between all cell components.

To better understanding the steel bending source and its impact in cell assembly, several tests were made: I) X-Ray diffraction (XRD); II) X-Ray photoemission spectroscopy (XPS); III) three cell operation tests with quartz window at same conditions; IV) pressure paper tests.

For XPS and XRD tests, first it is important to mention the steel type used for the flowfield frame. The steel type is X2CrNiMoN22-5-3 (with material number 1.4462) and it contains, beneath iron: 22.0% chromium; 5.5% nickel; 3.0% molybdenum; 0.03% carbon; 0.2% nitrogen. This specific steel type was chosen because it is highly stable against corrosion and can be formed better than most other stainless steels. The tests were made on two flowfield steel samples, one to the steel located in the active area (represented by a black circle in figure 20), which mean, the ribs, and the other to some part outside the active area (represented by a red circle in figure 20) and then compare the results between these two samples.

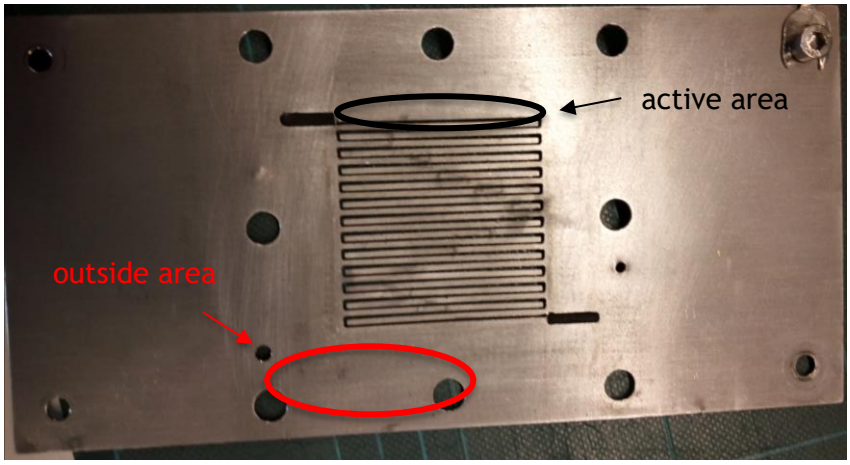

Figure 20. Active area and outside area samples.

I) X-Ray Diffraction (XRD)

X-Ray diffraction is a method for investigating the crystal lattice properties of materials. The material is exposed to X-rays and a detector is recording the intensity of X-ray reflexes for different angles. The radiation is reflected according to Bragg's law on the reflection on regular lattices (depending on the crystal lattice distance) [57]. From this reflection, is possible to calculate several crystal parameters as distance, crystal shape and crystallite expansion.

XRD spectra were recorded on a Bruker D8 Discover with areal detector (VÅNTEC 2000) and copper source (Cu-Kα, 8000 eV). The results are provided by two images, one is the raw data with the entire angle range (Appendix, Figure A.5.) and other focus on the angle range between 37.3º and 47º (Figure 21).

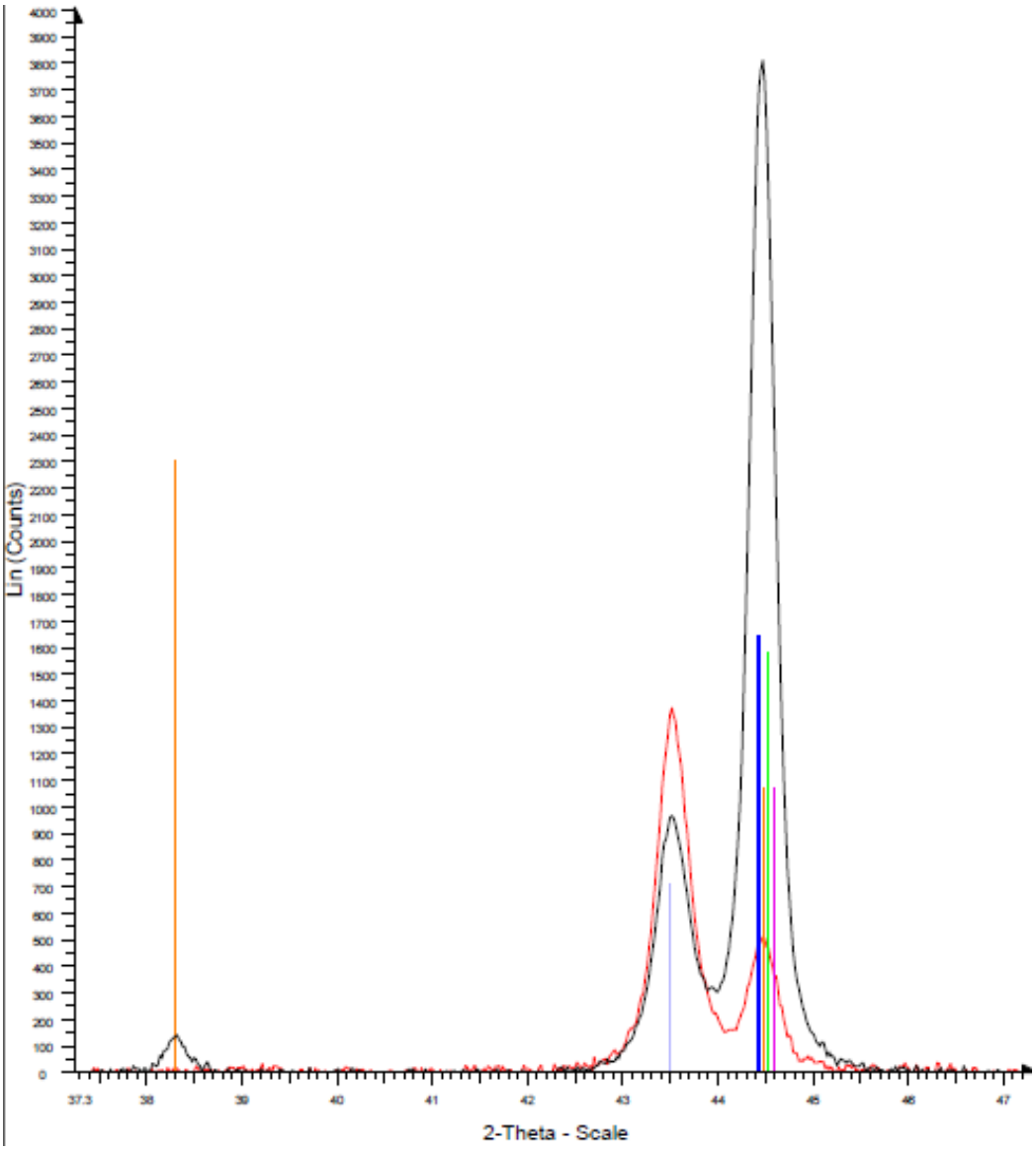

Figure 21. XRD measurement of the angle range between 37.3º and 47º. Black curve: Steel (active area); red curve: Steel (outside area); crystal lattice attributions from database: blue - Chromium; green - Iron Molybdenum alloy; pink - Chromium Nickel alloy; grey - Iron Nitride; orange - Gold.

In the XRD graph from Figure 21, black and red lines correspond to the active and outside areas, respectively. The vertical lines of different colours are related to the components that are constituent parts of steel that could be identified according to a lattice parameter database. A gold line was measured because in some previous tests a small piece of gold leaf was placed in the flowfield to understand if could be distinguished in IR images. As it is typical to observe more than one reflex, also reflexes of second or higher order at higher angles (compare with

Appendix, Figure A.5), it is possible to observe the gold reflex (orange line) first at 38.3º and second at 44.5º within the displayed range.

In 44.5º, the black reflex is much stronger than the red reflex. The black total reflex at 44.5º is partially the second gold reflex (notice that the gold signal at 44.5º is expected about 50% of the signal at 38.3º, indicated by the height of the orange line). The 44.5° reflex however, which is much more pronounced in the active area sample (black curve) than in the outside area sample (red curve), contains more signal, additional to gold. It can be attributed to some binary alloys of the elements present in this type of steel, according to a database included in the measurement software. A possible interpretation is, that some of the binary alloys may have formed out of the regular multiple alloy in the stainless steel.

A detailed analysis of the XRD spectrum was not made, as the results are not perfectly conclusive, but it proved that there was a modification from the outside area steel (original composition) and the steel composing the ribs and in direct contact with the reaction gases. It is concluded from the present data, that this type of steel is not suitable for the PEMFC application.

II) X-Ray photoemission spectroscopy (XPS)

X-Ray photoemission spectroscopy is a method to chemically analyse surfaces, exposing the samples to X-rays of low energy (for example Aluminium Kα radiation) in vacuum. The radiation ionizes the sample by emitting electrons out of inner electron shells of atoms; the emitted electrons suffer energy losses depending on the chemical state (oxidation state, chemical surrounding) of the atoms that can be derived [58]. As the energy levels are individual by each element, the elemental composition is visible in the spectra. XPS analysis just shows the surface composition. XPS were recorded using an Al Kα source with an energy of 1486.6 eV (Thermo Scientific ESCALAB 250) and a base pressure of $2x10^{-10}$ mbar. For the XPS tests were measured the two same samples measured in the XRD tests.

Image A.6. (Appendix) represents an overview spectrum, with all the expected elements of the steel type, Fe, Ni, Cr, N, C and typical surface contaminations (Ca, O, C, N). However, the chromium surface abundance is higher in the active area sample than in the outside area one, supporting the demixing observed in the XRD tests.

Figure 22 represents a closer view for regions around 400 eV, corresponding to the nitrogen 1s region. In this region is possible to directly compare the two samples spectrums by deconvolution of the signals.

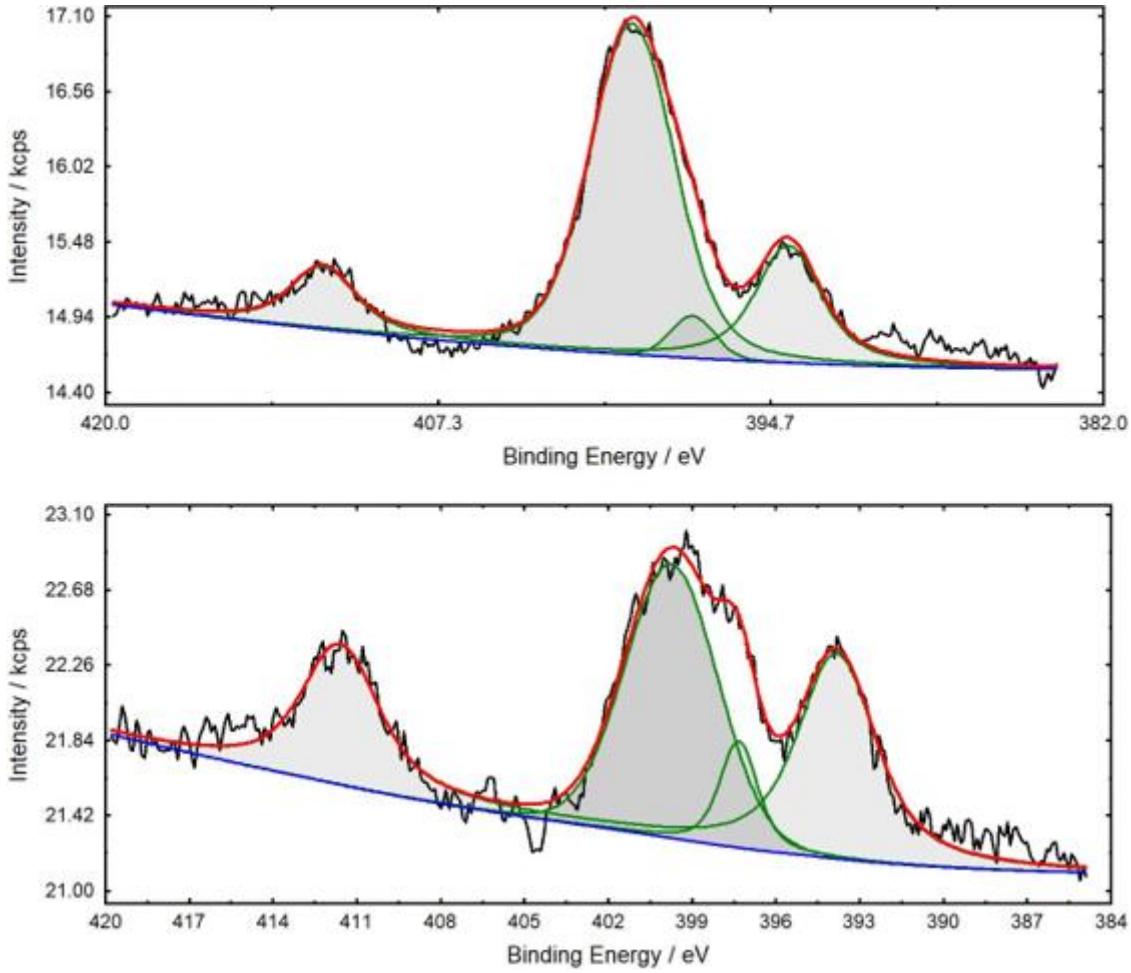

Figure 22. Closer spectroscopy measurement for the range between 384 and 420 eV. Top spectrum: active area; bottom spectrum: outside area.

There is the Nitrogen 1s signal at 398-400 eV and two Molybdenum side signals of the 4d electrons (393.5 and 411 eV). The Nitrogen 1s signal itself contains two compounds, a surface adsorbent (400 eV) and a smaller Nitride component (approximately 397.5 eV). Comparing the two samples, the ratio between this nitride component and the Molybdenum signals is not the same, which means that the active area sample has less of this nitride on the surface.

Similar to the XRD, the results were not conclusive but reinforce the finding that there were differences between the two samples, proving the idea that the steel in the active area is not completely identical anymore to the original steel type.

III) Cell with quartz window operation tests

For a better understanding of the impact that the flowfield plate bend had, the cell was operated with quartz window at exact same conditions as applied in the initial tests (see sub-chapter 4.1) and the values were compared. It was also made an intermedium operation with the same conditions, between these two tests. At that moment, the purpose of the intermediate cell test operation was to understand if the system was still obtaining satisfactory values. In Table 4 is represented the current density values obtained at 0.60, 0.55 and 0.50 V.

Table 4. Current density values for initial, intermediate and final tests at same conditions.

Test date	Current density values ($A \cdot cm^{-2}$)		
	0.60 V	0.55 V	0.50 V
October	0.46	0.58	0.70
December	0.30	0.36	0.43
January	0.00	0.00	0.00

The values observed in the table above demonstrate that the current density was decreasing over time and the final test shows no current, which proves that the flowfield stainless steel bending was critical to the point of obtaining no results. It is also possible to conclude that, with a progressive decreasing in current density, the bending was gradually increasing until it reached the point where it was no longer possible to obtain any current.

IV) Pressure papers tests

A test with pressure papers (FUJIFILM Prescale 4LW) was applied to visually understand the impact of the curvature of the flowfield plate. The pressure paper is composed of two polyester bases, one coated with a layer of micro-encapsulated colour-forming material and other with a layer of the colour-developing material, illustrated in Figure 23 [59]. The two coating layers should be in contact with each other and the two polyester bases outside.

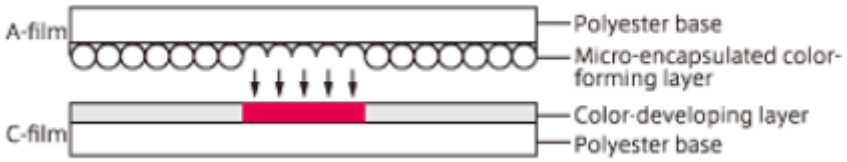

Figure 23. Two-sheet pressure papers type [59].

This test focused on how the flowfield plate bending could impact with the MEA contact with anode bi-polar-plate and the cathode flowfield frame. So, the pressure papers replaced the MEA and then the normal cell assembly occurs, at different torque values, to understand if all pressure area was in contact with the components or not. The two film papers were cut, in 8x8 cm pieces and placed where usually the MEA is placed. It was tested for 6 different torque values, from 1.5 to 4.0 N·m. The results are demonstrated in Figure 24. It is important to note that areas more coloured were areas that suffered more pressure. It is also important to distinguish two different areas, the active fuel cell area, visible as the square shaped area in the center, where usually the flowfield ribs are in contact with the GDL and the around area, where the ice cube gasket make contact with the flowfield stainless steel plate. The positions

of gas inlet and out are visible by the openings close to the upper left and lower right corners, each.

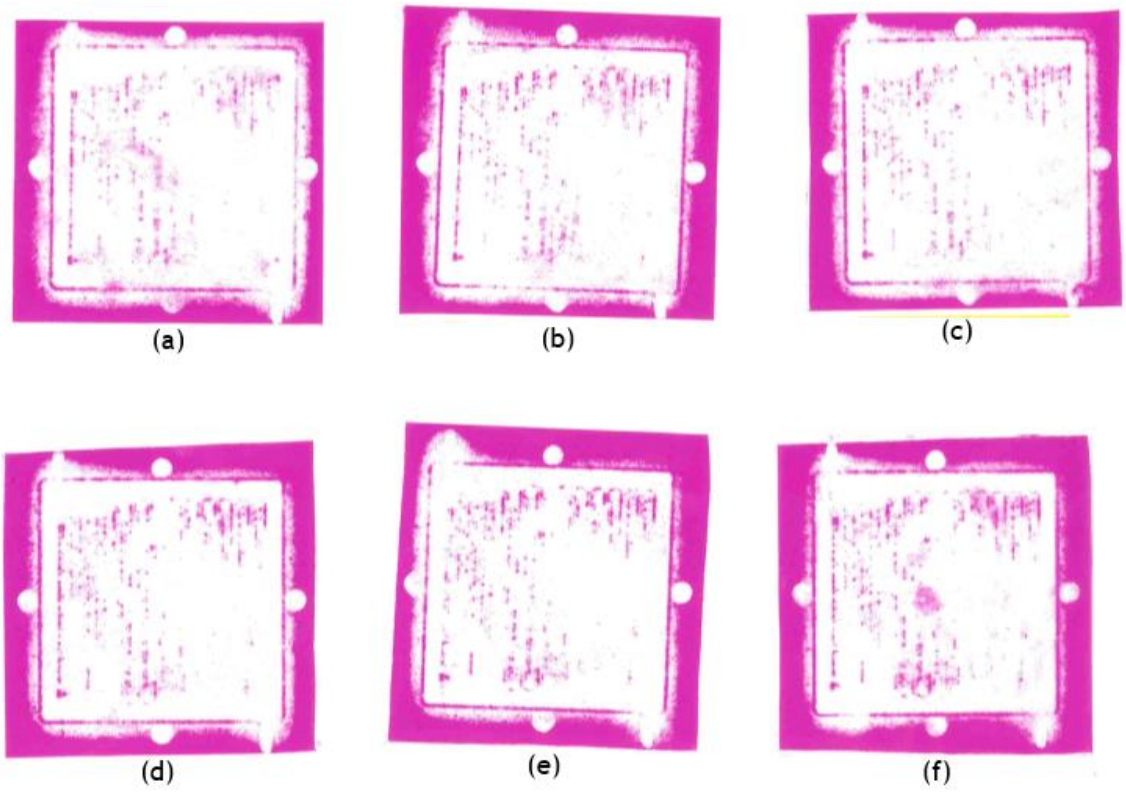

Figure 24. Pressure paper tests at different torques: (a) 1.5 N·m; (b) 2.0 N·m; (c) 2.5 N·m; (d) 3.0 N·m; (e) 3.5 N·m; (f) 4.0 N·m.

Observing the results, some conclusions can be made. In the 6 papers, it is possible to observe that the active area region, in general, is less colourful than the region around it, which means that the area corresponding to the ice cube gaskets have better contact with the cathode flowfield stainless steel frame than the active area of the cell. In the active area the tendency to lack of colour is visible in some specific regions: on almost all right half of the images and the on bottom left too, demonstrating that the flowfield did not establish a good contact with these regions, which is easily explained by the flowfield bending. Besides that, the asymmetry is a hint that the curvature of the flowfield is stronger on the right side than the left side. Lastly, it is possible to visualize the difference in the areas around the active area, where the top and bottom regions have worse contact than the side regions. It is also possible to differentiate the bottom left region, that remains with less colour regardless of the torque applied.

These observations allowed to better understand first, that the bending material had great impact in provide a good contact in the active area (between anode and cathode flowfields and the GDLs), and second, that the bending is not symmetric, which means that is more bent to the right side than the left side and more bent in the bottom region than in the top one. In any case, it was a permanent bend that stopped promoting good contact between the cell

components and, consequently, the reactant gases did not reach the catalyst sites in a proper way.

As the final conclusion these chapters, the stainless steel flowfield plate (steel type 1.4462) was identified as the weak part, as it bent continuously during the period of the experiments, most probably because of a structural change in the steel in the area of the electrochemically active area of the cell.

4.3 IR monitoring of fuel cell setup

As explained in the previous sub-chapter, it was impossible to obtain satisfactory fuel cell performance when the cell was assembled with the germanium window because of mechanical reasons only, so it was not possible to register IR images in operando. Nevertheless, some images in open circuit potential were observed and recorded with the present setup. By varying the inlet gases humidification and recording these IR images, it was possible to observe the evolution of the liquid water in the flowfield channels. Images of the entire area and more magnified images were obtained, without and with an additional germanium uncoated lens, respectively, to evaluate the potential of the advanced setup with antireflective coated Germanium windows.

In the IR images presented in the further sections, the ribs and channels can be easily distinguished because they have different emissivity values. The emissivity of the stainless steel is close to 0.77 and the emissivity of carbon is close to 0.97.

4.3.1 IR monitoring without magnification

The first IR images recorded by the IR camera were taken without the additional magnification lens, to have an overall flowfield image. The actual images with the native focal distance of the used camera captured the flowfield and part of the bi-polar plate, so it was necessary to cut the area cover by the bi-polar plate to obtain a better comparison between images (Figure 25).

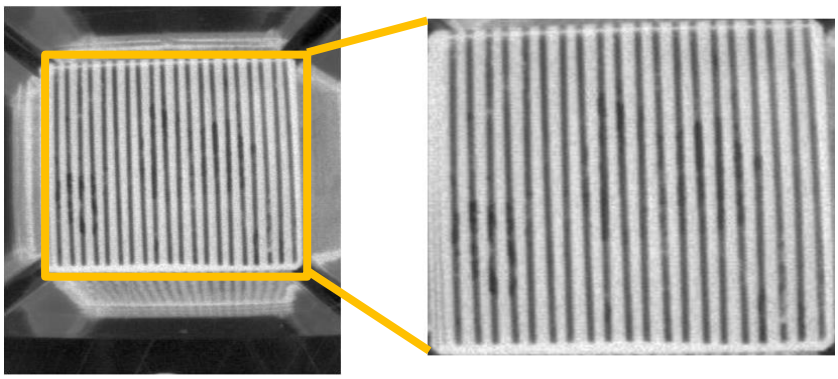

Figure 25. Image captured for IR camera without Ge lens.

The resolution of the IR camera is 360x240 pixels. The flowfield is composed of 25 channels and 24 ribs to cover the 5x5 cm cell active area. The area provided for the camera to capture IR images is 4x4 cm, so even for an overall flowfield image, just 20 channels and 20 ribs were captured. The image corresponding to the flowfield is 42% of the total image size and it is a square image, so it is possible to determine the pixels per lateral side. Thus, the intrinsic resolution is approximately 4.5 pixels per channel.

The cell was assembled and operated at pre-conditioning conditions (see section 3.1.6) excepted the relative humidification (RH), that was gradually changed and recorded over time from 50% (anode and cathode) to 100% RH, as illustrated in Figure 26.

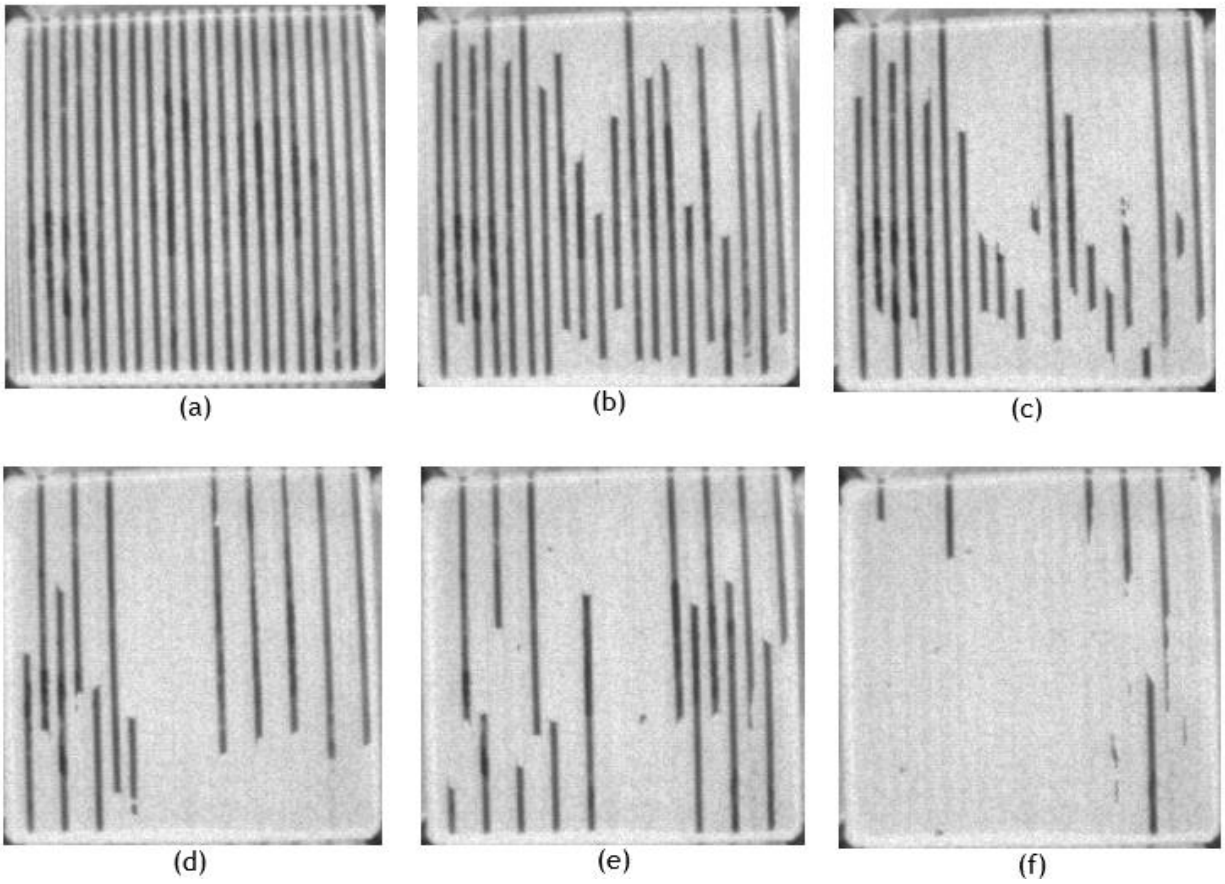

Figure 26. IR images for different anode-cathode % RH: (a) 52-50; (b) and (c) 65-65; (d) 75-78; (e) 91-96; (f) 100-100

In Figure 26, the black lines correspond to the channels and the grey lines to the ribs; the liquid water starts to appear in a light grey, barely distinguishable from the ribs. Observing these IR images, it is evident that the anti-reflective coating applied on the germanium window allows very good images since there is no reflection observed, and the high IR transmittance permits clear images. It was also possible to visualize the water appearance when it was increased the inlet gases humidification. From image to image, the black lines were less and less visible, as they are replaced by grey lines, with some remaining contrast to the ribs. Even for images

captured in open circuit potential and not in-operando, is possible to verify the potential for thermographic monitoring of liquid water formation and intrusion in PEMFC when a germanium window with anti-reflective coating is incorporated to the cell.

4.3.2 IR monitoring with magnification lens

As mentioned in sub-chapter 3.3, an uncoated germanium lens was placed in the camera with the help of a 3D printed polymer support (see Appendix, Figure A.3.). Figure 27 compares the two images, with and without the lens.

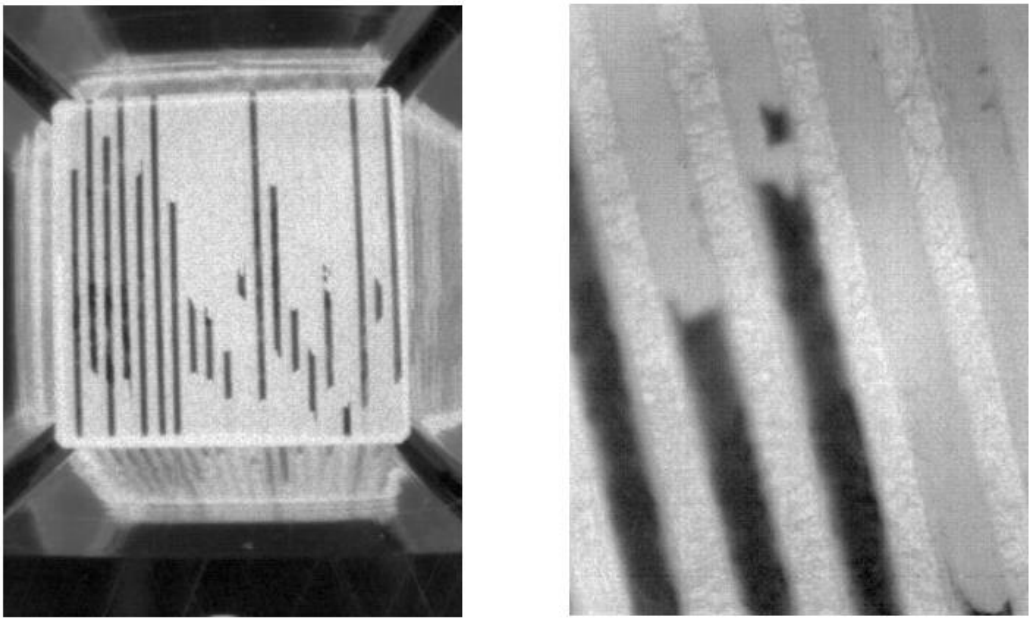

Figure 27. IR flowfield images without and with uncoated germanium lens, respectively.

In terms of magnification, the second image from Figure 33 corresponds to 240 pixels in the lateral expansion. The width of a channel corresponds to approximately 13% of the image, so the resolution of this image was around 30 pixels per channel. The magnification achieved with the addition of the germanium lens was around 6.5x comparing with the first picture from Figure 27.

As in the previous section, a sequence of images is shown below in Figure 28, also with the increasing of the inlet gases humidification over time, starting with the image with lower RH percentage (anode and cathode) to the image with higher RH percentage. The advancement of water (uniform grey) can be followed from image to image and is well resolved

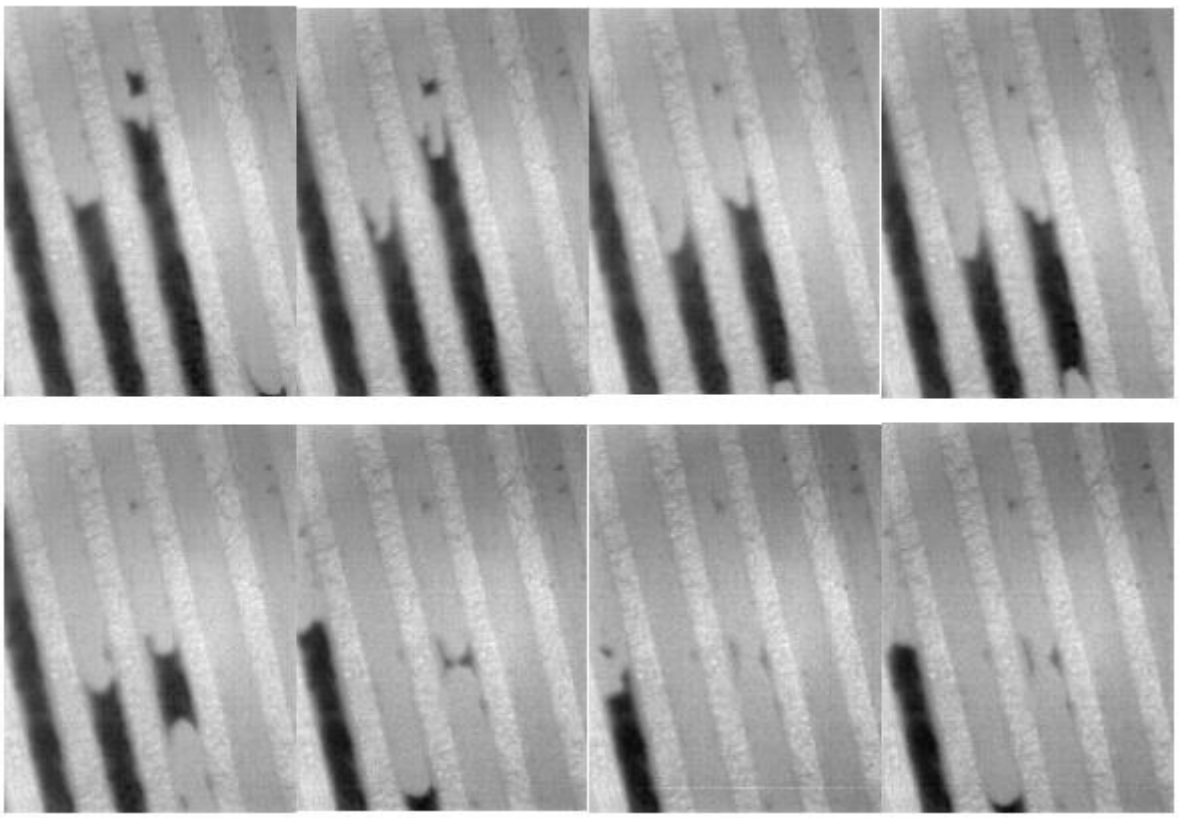

Figure 28. IR images with uncoated germanium lens for progressively more RH percentage.

Since these images were not captured in-operando, there was no preferred position to capture the magnified images. The camera was placed in a random position close to the window that allowed a sharp image. Before these images were taken, the camera with the lens was slowly moved until reach the position exposed in the images in Figure 28. Posteriorly, the camera was fixed in this position and this sequence of images was saved. As in images from Figure 32, in these images no reflection from the germanium window was observed, proving, once more, the benefits of using the anti-reflective coating germanium to perform thermography applications. With more magnified images, it is possible to understand better the water mobility through the channel. In several points along these images is possible to observe the water meniscus, providing a huge advantage in future studies of water management or transport of liquid water in the flowfield channels or water capillarity.

An anti-reflective coating germanium lens was not available in the laboratory. However, it is expected that better images can be achieved with this kind of lens since perform in general better results in optic systems.

5 Conclusion

5.1 Objectives Achieved

During this work the fuel cell concept to incorporate the germanium window, anti-reflective coated, was developed to show how the infrared imaging can be improved and can compete with other methods for detection of condensed water (for example neutron imaging). This work can be divided in three parts. First, the fuel cell with quartz window concept was operated, and it was possible to obtain a polarization curve, proving that this new fuel cell design principally works. In the second phase Second, the implementation of the germanium window, it was not successful to achieve stable fuel cell operation for operando imaging. The cause could be found in the bending of the stainless steel flowfield, which was increasing over time. Some tests were made to better understand and have some more information about the steel bending. X-Ray photoemission spectroscopy and X-Ray diffraction measurements were made, and hints were found concluded, that the steel structure of the "active" area exposed to the electrochemical reaction ambience changed over time. The slow distortion could be followed by the slow decay of the fuel cell performance. Three cell operation tests with quartz window at same conditions were made during this work, and the impact of the steel bending on performance over time led to conclude that, over time, the bend continuously increased. An additional experiment was made with pressure papers, a foil that is coloured by the force applied when placed inside the cell, to visually understand which MEA specific regions were poorly contacted. It can be concluded that the almost half right of the active area and the bottom left region are poorly contacted by the stainless steel flowfield, revealing the asymmetric bending. These four tests just strongly proof that the stainless steel flowfield plate (steel type 1.4462) was bending continuously during the experiments, with a structural change in the active area of the cell, demonstrating that this stainless steel type is not suitable for PEMFC application. The third and finally part demonstrates the IR monitoring in the assembled fuel cell with the anti-reflective coated germanium window, with and without magnification, however under open circuit voltage conditions only. Both experiments showed very promising results. Without magnification an overview of the flowfield is captured (with resolution of 4.5 pixels per channel). With magnification a closer view of the channels is possible, with resolution of 30 pixels per channel, that correspond to a magnification of 6.5x. Liquid water, channels, and ribs can be well distinguished, and even the meniscus of intruding water can be resolved. These IR images clearly demonstrate the benefits of the anti-reflective coating together with germanium, not detecting any reflectivity during the capture of IR images, and proving that this technology is a promising characterization and analysis tool for future applications.

5.2 Limitations and Future work

Due to the separation between the cathode bi-polar plate and the flowfield to incorporate the IR window, two additional sealings are needed. Even with the more stable quartz window, there were some leakages, so in order to study other conditions in operation with the IR camera, the sealing should be improved.

The main limitation during this work was the stainless steel flowfield continuously bending, turning it into a critical issue for the fuel cell operation. So, for further experiments with this fuel cell design, some possible alternatives could be coating the stainless steel with gold, or to build a flowfield plate from other metal (more stable for PEMFC application), for example titanium, or a thicker flowfield frame, to provide a better mechanically stability.

This initial work had the purpose of demonstrate the benefits of the anti-reflective coating germanium window for thermography applications, with a low-cost IR camera, in order to understand, first, if it is a viable technology to invest in the future, so the limitation with the camera sensitivity or resolution is obvious. Nevertheless, while not all potentialities could be explored, it is a characterization method worth the investment, not only for water distribution characterization. Also temperature distributions along and across the channels may be obtained, for example, to create a precise temperature profile and relate to the electrochemical reactions (that release heat) and simulation activities, with the final goals to optimize the local platinum loading through the whole active area, reducing the overall platinum loading towards a fuel cell with platinum gradients, exactly it is most needed for the reactant gases.

It could be possible to extend the thermography technology to PEM electrolyzers for example. Because of the higher temperature gradient and typically a simpler flow field, temperature profiles could possibly be characterized.

Lastly, if the spectral resolution is sufficient, it might be feasible to visualize the humidification level of gases in fuel cells, instead of only liquid water. As the contrast in IR radiation is given by the temperature and the emissivity of the materials, it would need to resolve the differences in emissivity.

5.3 Final Assessment

This work makes me grow intellectually and personally. In the academic, scientific field, it forces me to know more about different topics, as fuel cells, infrared radiation, optical, even about XPS or XRD, very different scientific areas, new to me, that provide me an important knowledge for my professional future. Personally, what this work taught me more was how to daily fight against the adversities without giving up, not matter the results. Also taught me that

sometimes it is acceptable to do not have the results intended, the important part is what I learn from it.

For this work in concrete, two important things: were proven first, the fuel cell with frame concept works; second, the benefits of the anti-reflective germanium coating, when compared to other infrared frames (for example, silicon, or uncoated germanium). During this work it was visible the assembly difficulties by incorporating the IR window, but more important it shows the contribution that thermography technology will have in future applications, not only in PEMFC, but it can extend for other electrochemistry applications, such as electrolyzers.

6 References

1. *International Energy Agency (IEA), Data and Statistics*. 2017.
2. Wilberforce, T., Alaswada, A., Palumbo, A., Dassistib, M., Olabia, A.G., International Journal of Hydrogen Energy, 2016. **41**(37): p. 16509.
3. Lipman, T.E., Weber, A.Z., *Fuel Cells and Hydrogen Production*. 2019: Springer New York
4. Silva, A., *Design of a Thermographic Setup and Applications to PEM Fuel Cells*, in *Chemical Engineering Department*. 2019, Faculty of Engineering of the University of Porto: Porto.
5. *"DLR Stuttgart at a glance"*.
6. IRENA (2018), *Hydrogen from renewable power: Technology outlook for the energy transition*. International Renewable Energy Agency, Abu Dhabi.
7. Konno, N., Mizuno, S., Nakaji, H., Ishikawa, Y., Int. J. Altern Powertrains. **4**: p. 123-129.
8. Kongkanand, A., Mathias, M., Journal Physical Chemistry Letters, 2016. **7(7)**: p. 1127-1137.
9. Friedrich, K.A., Stimming, U., Carrette, L., *Fuel Cells - Fundamentals and Applications*. 2001.
10. Pilatowsky, I., Romero, R.J., Isaza, C.A., Gamboa, S.A., Sebastian, P.J., Rivera, W., *Thermodynamics of Fuel Cells*. 2011.
11. Jung, C.-Y., Kim, W.-J., Yi, S.-C., International Journal of Hydrogen Energy, 2012. **37**: p. 7654-7668.
12. Azri, M., Khanipah, N.H.A., Ibrahim, Z., Rahim, N.A., International Journal of Power Electronics and Drive Systems, 2017. **8**(4): p. 1852-1862.
13. Oyarce, A., *Electrode degradation in proton exchange membrane fuel cells*, in *Applied Electrochemistry*. 2013, Kungliga Tekniska Högskolan Chemical Science and Engineering: Stockholm.
14. Nakamura, S., Nishikawa, H., Aoki, T., Ogami, Y., Journal of Power Sources, 2009. **186**: p. 278-285.
15. Xiea, Z., Zhaoa, X.S., Gazzarria; J., Wang, Q., Navessina, T., Holdcroft, S., ECS Transactions, 2009. **25 (1)**(1): p. 1187-1192.
16. Hwang, B., Lee, H., Park, K., Korean Chemical Engineering Research, 2017. **55**(4): p. 473-477.
17. James Larminie, J., Dicks, A., *Fuel Cell Systems Explained*. 2000: Wiley.
18. Solasi, R., Zou, Y., Huang, X., Reifsnider, K., Condit, D., Journal of Power Sources, 2007. **167(2)**: p. 366-377.
19. Khattra, N., Karlsson, A., Santare, M., Walsh, P., Busby, F., Journal of Power Sources, 2012. **214**: p. 365-376.
20. Khattra, N., Santare, M., Karlsson, A., Schmiedel, T., Busby, F., Fuel Cells, 2015. **15(1)**: p. 178-188.
21. Coulon, R., Bessler, W., Franco, A., ECS Transactions, 2010. **25(35)**: p. 259-273.

22. Yu, T., Sha, Y., Liu, W.G., Merinov, B., Shirvanian, P., Goddard, W. III, Journal of the American Chemical Society, 2011. **133(49)**: p. 19857-19863.
23. Jeon, S., Lee, J., Rios, G.M., Kim, H.-J., Lee, S.-Y., Cho, E., Lim, T.-H., Jang, J.H., Int. J. Hydrogen Energy, 2010. **35**: p. 9678-9686.
24. Godea, P., Jaouena, F., Lindbergha, G., Lundblada, A., Sundholm, G., Electrochimica Acta, 2003. **48**: p. 4175–4187.
25. Rashapov, R., Unno, J., Gostick, J., Journal Electrochem. Chem., 2015. **162(2)**: p. F603-F612.
26. Zenyuk, I.V., Parkinson, D.Y., Connolly, L.G., Weber, A.Z., Journal of Power Sources, 2016. **328**: p. 364-376.
27. Gostick, J.T., Ioannidis, M.A., Fowler, M.W., Pritzker, M.D., Electrochemistry Communications, 2009. **11(3)**: p. 576-579.
28. Malevich, D., Halliop, E., Peppley, B.A., Pharoah, J.G., Karan, K., Journal Electrochemical Society, 2009. **156(2)**: p. B216-B224.
29. Weber AZ, N.J., Journal Electrochemical Society, 2005. **152(4)**: p. A677-688.
30. Owejan, J.P., Owejan, J.E., Gu, W., Trabold, T.A., Tighe, T.W., Mathias, M.F., Journal Electrochemical Society, 2010. **157(10)**: p. B1456-B1464.
31. Thomas, A., Maranzana, G., Didierjean, S., Dillet, J., Lottin, O., International Journal of Hydrogen Energy, 2014. **39(6)**: p. 2649-2658.
32. Antunes, R., Oliveira, M., Ett, G., Ett, V., Journal of Power Sources, 2011. **196(6)**: p. 2945-2961.
33. Cunningham, B., Huang, J., Baird, D., International Materials Reviews, 2007. **52(1)**: p. 1-13.
34. Karimi, S., Fraser, N., Roberts, B., Foulkes, F., Advances in Materials Science and Engineering, 2012: p. 1-12.
35. Hornung, R., Kappelt, G., Journal of Power Sources, 1998: p. 72, 20.
36. Davies, D.P., Adcock, P.L., Turpin, M., Rowen, S.J., Journal of Power Sources 2000, 86, 237., 2000: p. 86, 237.
37. Tawfik, H., Hung, Y., Mahajan, D., 2007. **163(2)**: p. 755-767.
38. Antunes, R., Oliveira, M., Ett, G., Ett, V., International Journal of Hydrogen Energy, 2010. **35(8)**: p. 3632-3647.
39. Hermann, A., Chaudhuri, T., Spagnol, P., International Journal of Hydrogen Energy, 2005. **30(12)**: p. 1297-1302.
40. Lu, Z., Kandlikar, S., Rath, C., Grimm, M., Domigan, W., White, A., Hardbarger, M., Owejan, J., Trabold, T., International Journal of Hydrogen Energy, 2009. **34(8)**: p. 3445-3456.
41. Yan, Q., Toghiani, H., Wu, J., Journal of Power Sources, 2006. **158**: p. 316-325.
42. Janssen, G.J.M., Journal of Electrochemical Society, 2001. **148**: p. A1313-A1323.
43. Wu, Y., Cho, J.I.S, Whiteley, M., Rasha, L., Neville, T.P., Zieche, R., Xu, R., Owen, R., Kulkarni, N., Hack, J., Maier, M., Kardjilov, N., Markötter, H., Manke, I., Wang, F.R., Shearing, P.R., Breet, D.J.L., *Characterization of water management in metal foam flow-field based polymer electrolyte fuel cells using in-operando neutron radiography.* International Journal of Hydrogen Energy, 2019.
44. Sasabe, T., Tsushima, S., Hirai, S., International Journal of Hydrogen Energy, 2010. **35**: p. 11119-11128.

45. Ince, U.U., Markötter, H., George, M.G., Liu, H., Ge, N., Lee, J., Alrwashdeh, S.S., Zeis, R., Messerschmidt, M., Scholta, J., Bazylak, A., Manke, I., *Effects of compression on water distribution in gas diffusion layer materials of PEMFC in a point injection device by means of synchrotron X-ray imaging*. International Journal of Hydrogen Energy, 2017.

46. Bedeta, J., Maranzanaa, G., Leclerca, S., Lottina, O., Moynea, C., Stemmelena, D., Mutzenhardt, P., Canet, D., International Journal of Hydrogen Energy, 2008. **33**: p. 3146-3149.

47. Akhloufi, M.A., Bendadaa, A., *Fusion of active and passive infrared images for face recognition*. Proceedings of Spie, 2013. **8705**.

48. Tommaso Astarita, Giovanni Maria Carlomagno, *Infrared Thermography for Thermo-Fluid-Dynamics*. 2013: Springer.

49. Verdasca R, Simões R, *Current issues in medical thermography* 2013: Springer, Berlim.

50. Jones, B.F., *A Reappraisal of the Use of Infrared Thermal Image Analysis in Medicine*. IEEE Transations on Medical Imaging, 1998. **17**: p. 1019-1027.

51. Vollmer M, Möllmann K-P, *Infrared thermal imaging: fundamentals, research and applications*. 2011: Wiley, Weinheim.

52. C. Meola, S. Boccardi, G. M. Carlomagno, *Infrared Thermography in the evaluation of aerospace composite materials*. 2017: Elsevier.

53. *Powerful thermal imaging cameras*. [cited 2019 22 Jan]; Available from: https://www.thermal.com/compact-series.html.

54. *Geology Science. Quartz*. [cited 2020 23 January]; Available from: http://geologyscience.com/minerals/quartz/.

55. *Germanium windows*. [cited 2020 21 Jan]; Available from: https://www.knightoptical.com/stock/optical-components/infrared-optics/germanium-optical-components/germanium-windows/.

56. Korth Kristalle. *Germanium (Ge)*. [cited 2020 1 February 2020]; Available from: https://www.korth.de/index.php/162/items/14.html.

57. Bragg, W.H., Bragg, W.L., *The Reflection of X-Rays by Crystals*. Proceedings of the Royal Society of London. A., 1913. **88**(605): p. 428-38.

58. Einstein, A., Annalen der Physik, 1905. **322**(10): p. 891-921.

59. FUJIFILM. *Pressure Measurement Film - Prescale*. [cited 2020 28 Jan]; Available from: https://www.fujifilm.com/products/prescale/prescalefilm/.

A. Appendix

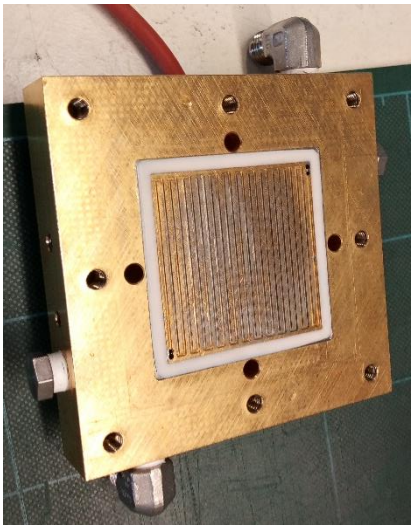

Figure A.1. Anode bi-polar plate with flowfield incorporated.

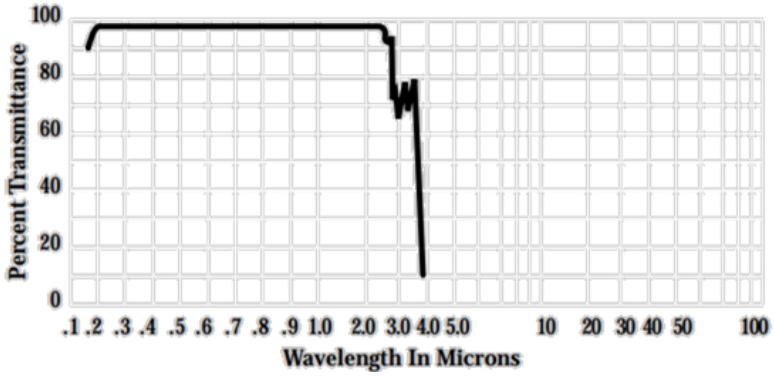

Figure A.2. Quartz glass transmission curve.

Table A.1. Quartz properties.

Properties of Quartz	
Refractive index at 3 µm	1.500
Transmission range (µm)	0.15 – 3.3
Thermal conductivity at 25 °C ($W \cdot m^{-1} \cdot °C^{-1}$)	6.82
Thermal Expansion at 20 °C ($°C^{-1}$)	13.24 x 10^-6
Density at 20 °C ($g \cdot cm^{-3}$)	2.649
Molecular Weight	60.06
Solubility in water ($g \cdot 100\ g^{-1}$ water)	Insoluble

Structure	Hexagonal

Table A.2. Properties of germanium crystal.

Properties of Germanium Crystal	
Refractive index at 11 μm	4.0026
Transmission range (μm)	1.8 – 14.0
Thermal conductivity at 293 K ($W \cdot m^{-1} \cdot K^{-1}$)	58.61
Thermal Expansion at 298 K (K^{-1})	6.1 x 10^-6
Density ($g \cdot cm^{-3}$)	5.33
Molecular Weight	72.59
Solubility in water ($g \cdot 100\ g^{-1}$ water)	Insoluble
Structure	FCC Cubic Diamond

Figure A.3. IR camera with uncoated germanium lens.

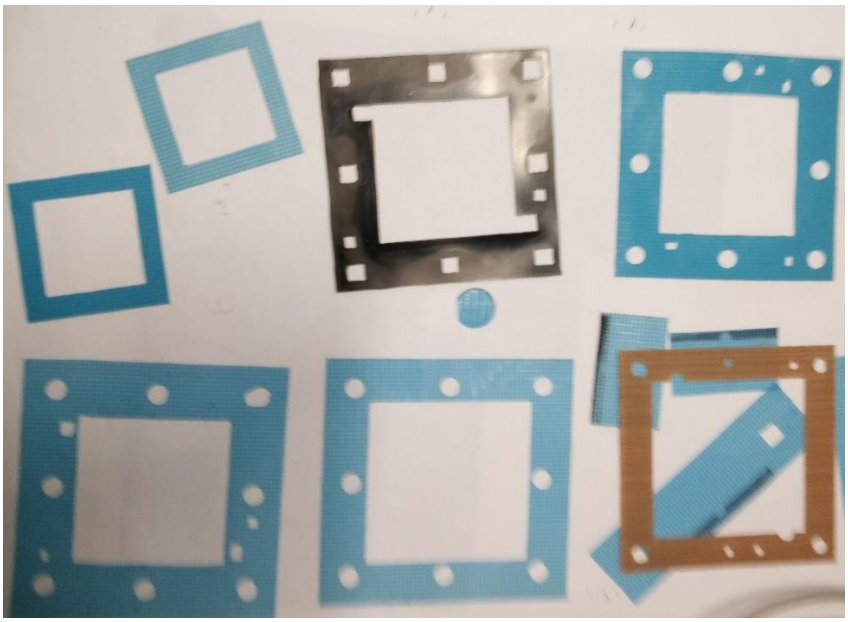

Figure A.4. Sealing materials (ice cube gasket in blue, Viton® in black and PTFE with fiberglass in brown).

Table A.3. Gases pressure tests for different sealing options.

Option	Sealings		Torque (N·m)	Real outlet pressure (bar)		Outlet pressure established (bar)
	Window	Flowfield		Anode	Cathode	
1	Icecube gasket 350 µm	Icecube gasket 350 µm	3.2	1.65	1.45	2.00
			3.5	1.85	1.70	
2	Icecube gasket 500 µm	Icecube gasket 350 µm	3.0	1.25	1.00	
3	Icecube gasket 500 µm	Icecube gasket 500 µm	3.0	1.50	1.40	
			3.2	1.65	1.50	
			3.5	1.80	1.70	
4	Icecube gasket 500 µm	PTFE 220 µm	3.0	1.35	1.05	
			3.2	1.35	1.05	
5	Icecube gasket 350 µm	PTFE 220 µm	3.0	1.25	1.10	
			3.2	1.26	1.10	
			3.5	1.30	1.15	
6	2 x icecube gaskets 350 µm	Viton 474 µm	3.0	1.27	1.14	
			3.2	1.30	1.17	
			3.5	1.33	1.21	
7	Icecube gasket 500 µm	Viton 474 µm	3.0	1.32	1.22	
			3.2	1.38	1.27	
			3.5	1.50	1.38	
8	2 x icecube gaskets 350 and 500 µm	Viton 474 µm	3.0	1.20	1.05	
			3.2	1.22	1.05	

Table A.4. Working and curing times for different Base/Catalyst weight ratios.

Base/Catalyst weight ratio	Working time (h)	Curing time (h)
5:1	1	5
10:1	2	7
20:1	3	12

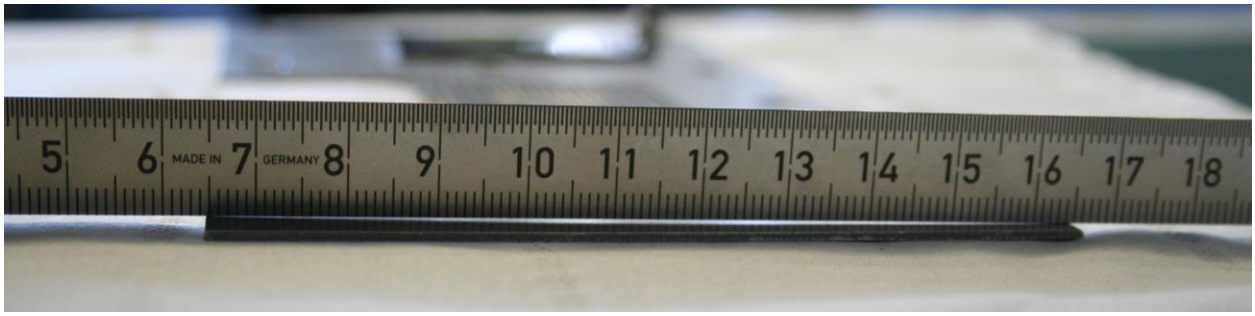

Figure A.5. Stainless steel flowfield plate bend.

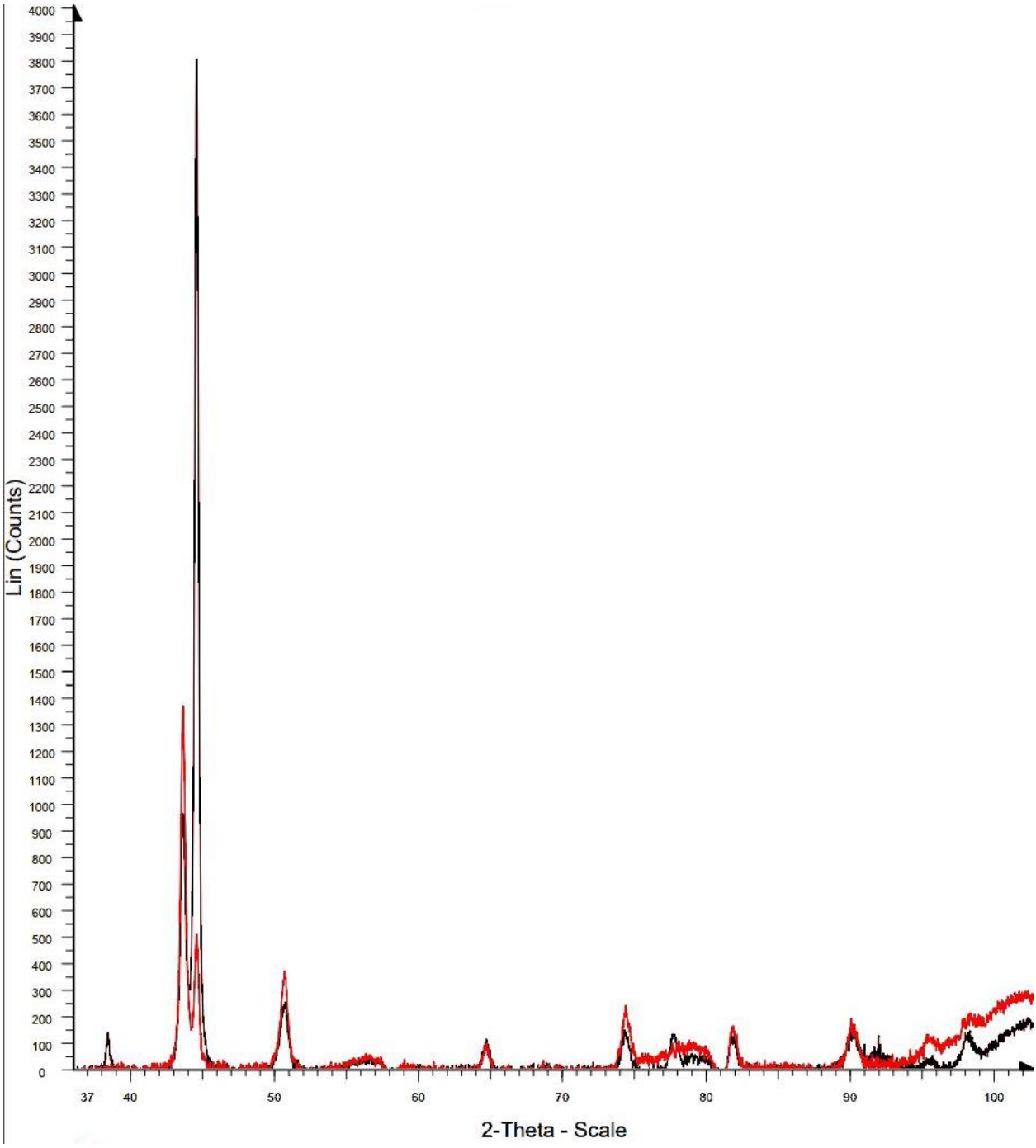

Figure A.6. XRD measurement with the entire angle range (black: active area; red curve: outside area).

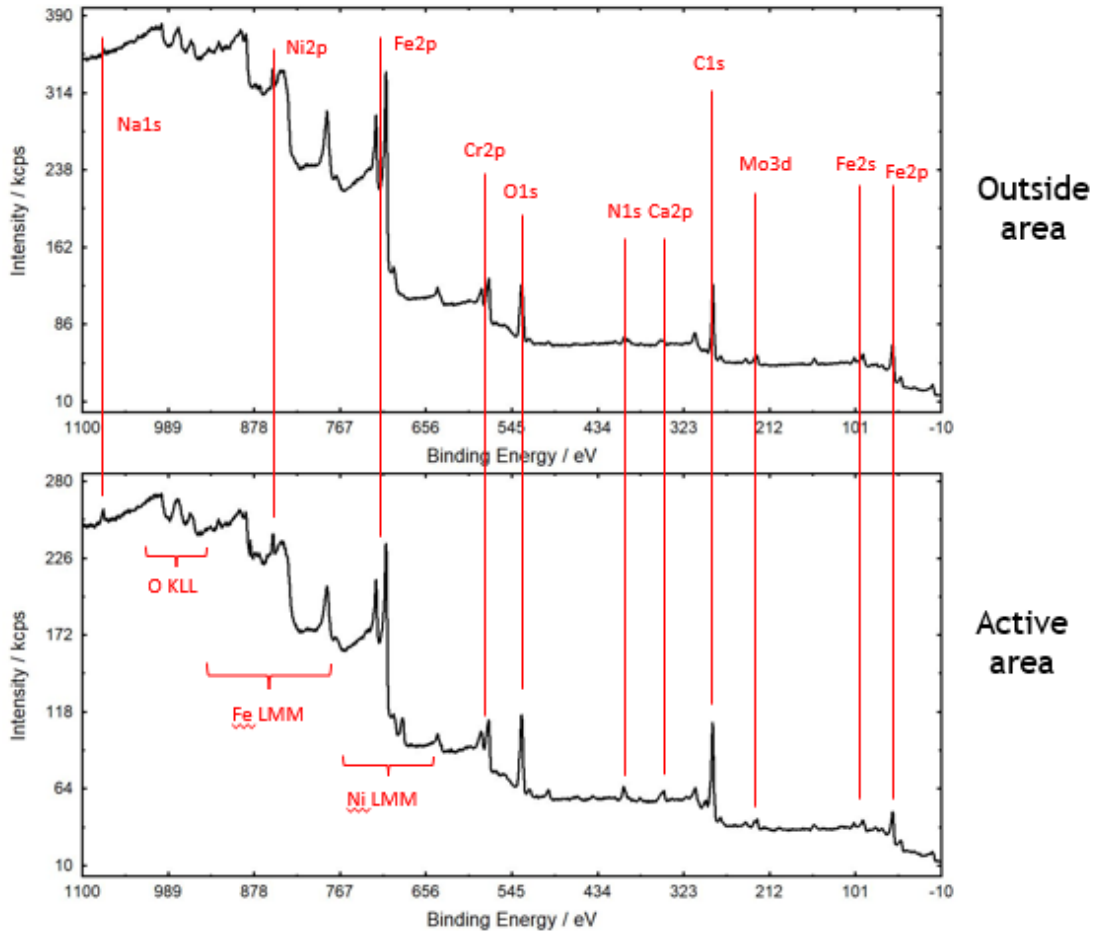

Figure A.7. Overview spectrum for two flowfield steel samples (outside and active area).